Thermo-hydraulic analysis of desiccation cracked soil strata considering ground temperature and moisture dynamics under the influence of soil-atmosphere interactions

Authors' affiliation:

Name: Milad Jabbarzadeh
Affiliation: MSc. Student
Address: Department of Civil Engineering, Sharif University of Technology, Tehran, Iran
E-mail: milad.jabbarzadeh@sharif.edu

Name: Hamed Sadeghi* (Corresponding author)
Affiliation: Assistant Professor
Address: Department of Civil Engineering, Sharif University of Technology, Tehran, Iran
E-mail: hsadeghi@sharif.edu
Tel: +98(21)6616-4208

Name: Saeed Tourchi
Affiliation: MSCA Postdoctoral Fellow
Address: Institute of Hydrogeology, Engineering Geology and Applied Geophysics, Faculty of Science, Charles University, Prague, Czech Republic.
E-mail: tourchis@natur.cuni.cz

Name: Ali Golaghaei Darzi
Affiliation: PhD Student
Address: Department of Civil Engineering, Sharif University of Technology, Tehran, Iran
E-mail: ali.golaghaei@sharif.edu

Preprint submitted to EarthArXiv (non peer-reviewed)

Thermo-hydraulic analysis of desiccation cracked soil strata considering ground temperature and moisture dynamics under the influence of soil-atmosphere interactions

Milad Jabbarzadeh, Hamed Sadeghi[*], Saeed Tourchi, Ali Golaghaei Darzi

Abstract

Global warming and climate change significantly affect ground temperature and flow patterns. Moreover, areas prone to cracking experience intensified temperature and moisture variations. Therefore, the aim of this study is to investigate ground temperature and moisture dynamics considering soil-atmosphere interaction through a coupled thermo-hydraulic analysis. Heat transfer, advective, and non-advective fluxes were simulated using CODE_BRIGHT finite element program to study water flow and energy transfer within the soil. Statistical analyses were conducted using an existing dataset to match the crack geometry with previous studies and find the best distribution for the width-to-depth ratio of cracks (C_R) as a dimensionless parameter. The results indicated that C_R variations follow a lognormal distribution. Numerical modeling scenarios were developed using statistical analysis results. The findings indicate that temperature variations decrease exponentially with depth, while surface soil temperature shows higher uncertainty due to atmospheric temperature fluctuations. Collecting various temperature trends in cracked soil at different time intervals, defined a limited region as maximum range of temperature variations (ΔT). Results reveal that ΔT in different crack scenarios can vary up to 4 times higher than intact soil. For the prediction of ΔT, considering the impact of climate variations on cracked soil, a 3D boundary surface was developed based on two variables: soil depth (z) and crack depth (C_D). Furthermore, an equation for estimating ΔT for uncracked soils was proposed. Additionally, cracked soil showed approximately 1.4 times higher desiccation

[*] Corresponding Author: hsadeghi@sharif.edu

rates than uncracked soil. Deeper cracks exhibited even more severe desiccation rates, being about 1.2 times higher.

Keywords: Thermo-hydraulic analysis; Soil desiccation cracking; Soil-atmosphere interaction; Ground temperature fluctuations; Soil moisture dynamics.

1. Introduction

Global warming has emerged as a significant concern in recent years, with its far-reaching impacts being felt across various fields, including soil science. One notable consequence of global warming is the rise in ground temperature, impacting geotechnical aspects like geothermal energy extraction.[1,2] Geothermal systems, like ground source heat pumps (GSHP) utilise the natural heat stored within the ground for heating and cooling purposes, offering an energy-efficient and sustainable alternative to traditional fossil fuel-based systems.[3-7] However, the changing climate and associated phenomena challenge the efficient operation of geothermal systems.[8] The importance of comprehending ground temperature fluctuations becomes evident when considering specific applications. For instance, in the design and operation of underground infrastructure, such as underground cables or pipelines, temperature variations can impact their structural integrity and performance. In agricultural practices, precise knowledge of ground temperature variations also helps optimise crop growth, irrigation strategies, nutrient availability, and microbial activity.[9-11] Moreover, soil temperature influences the rate of organic matter decomposition and mineralisation of organic materials.[12]

Soil desiccation cracking is an indirect result of global warming and the subsequent changes in soil moisture content and temperature. The thermal radiation-induced changes in water-saturated soil increase the kinetic energy of water molecules[13], leading to evaporation and subsequent soil drying. Soil suction, also known as negative matric potential, represents the energy change per unit volume of water when transferred from the soil to the free water state.[14]

The drying process induces increased matric suction, which generates tensile stress that can surpass the soil's tensile strength and ultimately lead to the formation of desiccation cracks.[15,16] Furthermore, the tensile strength is influenced by the degree of saturation.[17] From a fracture energy perspective, cracks tend to form in a manner that minimises fracture energy release by efficiently creating new solid surfaces with the same amount of accumulated strain energy during desiccation.[18] As desiccation progresses, the network of cracks becomes stable, and no new cracks are formed. Instead, the existing cracks widen further.[19] Cracks significantly impact soil thermo-hydraulic (TH) behaviour by facilitating water movement and heat transfer, thereby accelerating the drying process by creating preferential pathways.[20] During dry periods, desiccation cracks facilitate evaporation by providing direct pathways for moisture to escape from the soil surface. This increases water loss and reduces soil moisture content, affecting the overall hydrological balance. Additionally, when heavy rainfall occurs following a dry spell, the existing desiccation cracks act as conduits for water infiltration, potentially altering the soil's hydraulic properties and moisture distribution.

Based on recent studies, the formation and propagation of cracks have been extensively investigated, including field observations[21-24], laboratory experiments[25-30], and numerical simulations[31-36]. Besides, numerous studies have focused on the soil-atmosphere interaction[37-40], particularly the influence of cracks on surface evaporation.[41-46] It was found that turbulent air movement within shrinkage cracks significantly impacts evaporation, even with a constant vapour pressure deficit above the crack aperture.[47] A significant increase in evaporation from moist cracked soil was observed, with a 60% to 65% higher evaporation rate than intact soil.[45] Similarly, a 12% to 16% increase in evaporation from bare soil due to the presence of cracks was reported.[48] Various studies have also demonstrated that the evaporation rate from crack opening is a proportion of the evaporation rate from the soil surface. This proportion has been reported at different values, ranging from 30% to 60%.[41-43] Therefore, existing studies generally agree on the increased evaporation rate due to soil cracking. However, these studies have limitations in properly acknowledging the variations caused by different crack geometries, spatial arrangements, and resulting water flow regimes. Moreover, these studies do not consider the moisture distribution and rate of soil dryness in both surface and deeper soil depths. Besides, desiccation cracks influence heat transfer within the soil. As the cracks develop, they create channels for enhanced air circulation, affecting thermal conductivity and heat exchange processes. This can result in intensified ground temperature fluctuations and irregular heat distribution within the soil profile, impacting the overall energy balance at the soil surface. The reduced moisture content in cracked soil also leads to decreased thermal conductivity, further contributing to temperature variations.

Although the ground temperature and moisture dynamics have various applications in different fields, further investigations are needed to understand their variations in clay layers susceptible to desiccation cracking, considering climate changes and global warming. Cracks induce moisture redistribution with flow regime changes in cracked regions during seasonal climate variations, leading to alterations in the soil drying pattern. These long-term changes in soil moisture distribution can significantly impact ground temperature profiles to considerable depths, making them relevant for planning, designing, and evaluating the performance of underground infrastructures and biogeomechanics purposes. Hence, the objective of this research is to investigate desiccation cracked soil temperature and moisture dynamics, considering soil-atmosphere interaction. This will be accomplished by analysing different modeling scenarios that take into account various predefined crack geometries and spacing. The scenarios are achieved through rigorous statistical analysis of diverse data sets containing crack dimensions on desiccated soils. The study employed a coupled thermo-hydraulic numerical analysis of the soil-atmosphere interaction problem using the CODE_BRIGHT program.

2. Material and methods

To conduct the simulations, it is essential to calculate the influxes and outfluxes in the soil medium, such as infiltration and evaporation, by analysing the soil-atmosphere interactions. These fluxes can occur in three modes: energy, water, and gas exchange. They result in changes in the mass and energy balance at the soil surface, which need to be continuously accounted for by solving the balance equations. Additionally, determining the total fluxes is crucial for solving these equations, as they consist of both advective and non-advective components. Therefore, defining the governing constitutive equations for the problem is necessary. To indicate this relationship between the balance and the constitutive equations for an unsaturated porous medium, a flowchart, as shown in Fig. 1, is provided. By solving these equations, the unknowns of the balance equations are determined, leading to the solution of the coupled thermo-hydraulic problem. In the following, the governing equations for the problem are presented, including the balance equations, constitutive equations, and equations related to soil-atmosphere interactions.

2.1 Balance and constitutive equations

Analysing porous media under atmospheric conditions requires considering the mutual interactions between different factors. One important aspect is the thermal expansion of water in the pores, which affects saturation degree and water pressure. Additionally, thermal-induced vapour diffusion has a significant impact on water transfer. These mutual influences between water and heat transfer are key factors that must be considered.[49-51] The theoretical framework employed in this study utilises a multiphase and multispecies approach. Phases are distinguished using subscripts (s: solid, l: liquid, g: gas), while species are identified using superscripts (w: water, a: dry air). A compositional approach[52] was used to formulate mass balance equations, which balance species rather than phases.[53,54] The formulation's central component comprises two balance conditions corresponding to equations for water mass balance and internal energy balance. These two conditions must be solved simultaneously to account for the interdependent interactions between various phenomena accurately. Then, the formulation is further complemented by a set of constitutive equations and an equilibrium restriction.

2.1.1 Mass balance of water

Water is considered a species in all three phases: solid, liquid, and gas, within a porous medium. This implies that water can be as adsorbed water on solid surfaces, as liquid water fills the pore spaces and water vapour occupies the void spaces within the medium.[55] Hence, the total mass balance of water can be expressed as:[53,54]

$$\frac{\partial}{\partial t}\left(\left(\omega_l^w \rho_l S_l + \omega_g^w \rho_g S_g\right)\phi\right) + \nabla \cdot \left(\mathbf{j}_l^w + \mathbf{j}_g^w\right) = f^w \tag{1}$$

where ω is mass fraction, ρ is mass content per unit volume of phase, S is degree of saturation, ϕ is porosity, $\mathbf{j}$ is total mass flux and f^w is an external supply of water. The water mass balance equation excludes internal supply, focusing solely on the total mass balance within the medium. By solving this equation, assessing the dynamics and distribution of pore water within the soil voids becomes feasible.

2.1.2 Energy balance

While in most cases, the energy balance is simplified to an enthalpy balance, it can also be expressed in terms of internal energy. Assuming thermal equilibrium between phases and uniform temperature across all phases, a single equation of total energy is sufficient.[56] Therefore, the internal energy balance for the porous medium by considering the internal energy within each phase can be written as:[53,54]

$$\frac{\partial}{\partial t}\left(E_l \rho_l S_l \phi + E_g \rho_g S_g \phi\right) + \nabla \cdot \left(\mathbf{i}_c + \mathbf{j}_{El} + \mathbf{j}_{Eg}\right) = f^E \tag{2}$$

where E_l and E_g are specific internal energy corresponding to each phase, $\mathbf{i}_c$ is energy flux due to conduction through the porous medium, $\mathbf{j}_{El}$, and $\mathbf{j}_{Eg}$ are advective fluxes of energy caused by mass motions and f^E is an internal or external energy supply.

2.1.3 Constitutive equations and equilibrium restriction

The constitutive equations establish the relationship between the independent variables (unknowns) and dependent variables.[46] When these constitutive equations are substituted into the balance equations, the governing equations are expressed in terms of the unknowns. Darcy's law is defined for the advective flow of liquid and gas phases, due to total head difference, within a porous medium:

$$\mathbf{q}_\alpha = -\frac{\mathbf{k} k_{r\alpha}}{\mu_\alpha}\left(\nabla P_\alpha - \rho_\alpha \mathbf{g}\right) \tag{3}$$

where $\mathbf{k}$ (m^2) is the intrinsic permeability tensor, $k_{r\alpha}$ is the relative permeability, μ_α (Pa.s) is the dynamic viscosity, P_α (Pa) is the pressure, and $\mathbf{g}$ is the gravity vector. The letter α can represent either l or g, depending on the phase it is describing. The intrinsic permeability tensor, as the primary parameter determining the advective flow of liquid and air, is defined by the Kozeny equation in terms of the porosity for a continuum medium as:

$$\mathbf{k} = \mathbf{k}_o \left(\frac{\phi}{\phi_0}\right)^3 \left(\frac{1-\phi_o}{1-\phi}\right)^2 \tag{4}$$

where ϕ_o is the reference porosity, $\mathbf{k}_o$ (m^2) is the intrinsic permeability which is assumed isotropic at the reference porosity. Several studies have reported Boom clay intrinsic permeability between 1×10^{-19} m^2 and 5×10^{-19} m^2.[57-61] In this study, the isotropic intrinsic permeability of Boom clay is considered as 2.5×10^{-19} m^2. In addition, to compute the liquid phase relative permeability, the van Genuchten-Mualem model is employed which expresses the variation of permeability with the degree of saturation:[62,63]

$$k_{rl} = \sqrt{S_e}\left[1 - \left(1 - S_e^{1/\lambda}\right)^{\lambda}\right]^2 \tag{5}$$

where λ is the shape parameter, and S_e is the effective liquid saturation defined in terms of the residual liquid saturation S_{rl} and the maximum liquid saturation S_{ls}. Notably, as the degree of saturation decreases, the water meniscus radius decreases, resulting in increased water potentail or soil suction $(P_{\mathrm{g}} - P_l)$. It is important to emphasise that this effect becomes particularly prominent when dealing with suctions in the capillary range. The soil-water retention and hydraulic conductivity, crucial parameters in unsaturated porous media, can be significantly influenced by various hydraulic properties, such as pore fluid chemistry and thermal conditions.[64-66] For the establishment of the relationship between suction and saturation degree, the van Genuchten model[62] is employed to characterise the soil-water retention curve (SWRC) which has an important impact on unsaturated flow:

$$S_e = \frac{S_l - S_{rl}}{S_{ls} - S_{rl}} = \left[1 + \left(\frac{P_{\mathrm{g}} - P_l}{P_0\ (\sigma/\sigma_0)}\right)^{\frac{1}{1-\lambda}}\right]^{-\lambda} \tag{6}$$

where P_0 (Pa) is the air entry value, σ (N/m) is the surface tension at a temperature T (°C), and σ_0 is the surface tension at a temperature at which P_0 is measured. In this study, the surface tension is assumed to be 0.072 N/m, based on the measured air entry value of 3.44 MPa. Additionally, the shape parameter is set to 0.3, following the findings reported by Delahaye and Alonso.[67] To calculate the relative permeability of the gas phase, the generalised power method is utilised:

$$k_{rg} = AS_{eg}{}^{\lambda} \tag{7}$$

$$S_{eg} = \frac{S_g - S_{rg}}{S_{gs} - S_{rg}} \tag{8}$$

where A is a constant, λ is the model parameter and S_{eg} is the effective gas saturation. Based on the definition of fluid phase saturation ($S_l + S_g = 1$), S_{rg} and S_{gs} are defined as $1 - S_{rl}$ and $1 - S_{ls}$, respectively.

Fick's law explains the diffusion process in the system, encompassing water vapour diffusion in the gas phase and air diffusion in water. It allows for the computation of non-advective fluxes of species within the fluid phases, including molecular diffusion and mechanical dispersion. In this study, Fick's law is used to express the water vapour diffusion in the gas phase:

$$\mathbf{i}_g^w = -\left(\tau \phi \rho_g S_g D_g^w \mathbf{I}\right) \nabla \omega_g^w \tag{9}$$

$$D_g^w = D\left(\frac{(273.15 + T)^n}{P_g}\right) \tag{10}$$

where τ is the tortuosity coefficient which is defined as a constant value ($\tau = \tau_0$), D_g^w (m^2/s) is the diffusion coefficient of vapour in the air, $\mathbf{I}$ is the indentity matrix, D and n are model parameters. The primary mechanisms of energy transfer in a porous medium involve conduction, advection resulting from mass flux, and phase change.[56,68] Therefore, to consider heat transfer, Fourier's law is employed to calculate the conductive heat flux:

$$\mathbf{i}_c = -\kappa \nabla T \tag{11}$$

where κ (W/mK) is the thermal conductivity of the porous media. The overall thermal conductivity decreases with increasing porosity and decreasing degree of saturation. Moreover, thermal conductivity of a multiphase medium is influenced by the microstructural arrangement of the material, leading to an average value that combines the conductivities of the individual phases.[38] For intermediate phase arrangements, the weighted geometric mean of thermal conductivities provides a reliable estimate:

$$\kappa = \kappa_s^{(1-\phi)} \kappa_l^{\phi S_l} \kappa_g^{\phi(1-S_l)} = \kappa_{sat}^{S_l} \kappa_{dry}^{1-S_l} \tag{12}$$

where κ_{sat} and κ_{dry} (W/mK) are the thermal conductivity of the saturated and dry porous medium, respectively. A linear relationship between thermal conductivity and the degree of soil saturation is approximated as follows:[69]

$$\kappa = 0.7936\, S_l + 0.646 \tag{13}$$

From the above equation, the thermal conductivity corresponding to the saturated condition (S_l = 1) is κ_{sat} = 1.4396 and dry condition (S_l = 0) is κ_{dry} = 0.646.

It is assumed that phase changes, such as water evaporation, occur quickly compared to the characteristic timescales of the problem. As a result, these phase changes can be considered to reach local equilibrium rapidly. This assumption leads to an equilibrium restriction that must always be satisfied.[56] Hence, the psychrometric law is used to obtain vapour concentration in the gaseous phase (θ_g^w) as an equilibrium restriction:

$$\theta_g^w = \left(\theta_g^w\right)^0 \exp\left[\frac{-(P_g - P_l)M_w}{R(273.15+T)\rho_l}\right] \tag{14}$$

where M_w is the water molecular weight (0.018 kg/mol), R is the universal gas constant (8.314 J/(mol.K)), and $\left(\theta_g^w\right)^0$ is the saturated vapour concentration in the gas phase in equilibrium with a liquid with a flat surface at the same temperature, defined as:

$$\left(\theta_g^w\right)^0 = \frac{M_w P_{v(T)}}{R(273.15+T)} \tag{15}$$

$$P_{v(T)} = 136075 \exp\left[\frac{-5239.7}{273.15+T}\right] \tag{16}$$

where $P_{v(T)}$ (Pa) is the saturated vapour pressure. In Table 1, defined constitutive equations and model input values are summarised.

2.2 Soil-atmosphere interaction

Soil-atmosphere interaction refers to the dynamic exchange of energy, water, and gases between the soil surface and the surrounding atmosphere.[37] The soil-atmosphere interface is a critical boundary where heat, moisture, and gases are transferred through complex mechanisms such as evaporation, transpiration, and gas diffusion.[39,40]

The adopted model incorporates atmospheric variables, including temperature, precipitation, wind speed, relative humidity, and radiation. Subsequently, it calculates the water fluxes (via gas and liquid phases) driven by evaporation and rainfall, the air and energy fluxes encompassing radiation, advective effects, and convective energy fluxes. The following section explains the governing equations of soil-atmosphere interaction.

2.2.1 Mass fluxes of gas and water

The advective air flux (j_a) is utilised in the gas phase and defined as:

$$j_a = \omega_g^a q_g = \left(1 - \omega_g^w\right)\gamma_g\left(P_g - P_{ga}\right) \tag{17}$$

where q_g is the flux of the gas phase, P_{ga} (Pa) is the atmospheric pressure and γ_g is the leakage coefficient. The calculation of evaporation (E) involves an aerodynamic diffusion relation, as follows:[70-72]

$$E = \frac{1}{r_a}(\rho_{va} - \rho_v) = \frac{k^2 v_a \varphi}{\left(\ln \frac{\mathrm{z_a}}{\mathrm{z_0}}\right)^2}(\rho_{va} - \rho_v) \tag{18}$$

where r_a (s/m) is the aerodynamic resistance of air, k is the von Karman's constant, φ is the stability factor, v_a (m/s) is the wind speed, $\mathrm{z_0}$ (m) is the ground surface roughness length, $\mathrm{z_a}$ (m) is the screen height at which v_a and ρ_{va} are measured, ρ_{va} and ρ_v (kg/m^3) are the vapour mass per volume of the gas of the atmosphere and ground, respectively. Therefore, to define the movement of vapour induced by water evaporation through the soil pores or air-filled spaces driven by pressure difference, the advective flux of vapour by the gas phase is defined as:[72]

$$\begin{cases} j_g^w = \omega_g^w q_g & \text{if} \quad P_g > P_{ga} \\ j_g^w = \dfrac{\rho_{va}}{\rho_{ga}} q_g & \text{if} \quad P_g \leq P_{ga} \end{cases} \tag{19}$$

where ρ_{ga} is the atmospheric air density. When considering rainfall effects, it is important to mention that water flows over the land surface due to precipitation may exceed the soil's infiltration capacity. In this case, the shallow soil becomes saturated ($P_l > P_{ga}$), and any rainfall that cannot infiltrate will result in runoff. The surface runoff (j_{sr}) represents the rate at which water flows through the liquid phase is written as:[72]

$$\begin{cases} j_{sr} = \gamma_w \left(P_l - P_{ga} \right) & \text{if} \quad P_l > P_{ga} \\ j_{sr} = 0 & \text{if} \quad P_l \leq P_{ga} \end{cases} \tag{20}$$

where γ_w is the water leakage coefficient. It is important to note that the simulation does not explicitly account for ponding. When assuming no ponding, a sufficiently high value for γ_w can be utilised (while avoiding numerical instabilities). Finally, the total water flux (j_w) is expressed as the sum of previously defined parameters, as follows:

$$j_w = k_{rain} P + k_{evap} E + j_g^w + j_{sr} \tag{21}$$

where P is the rainfall, k_{rain} and k_{evap} are the coefficients that can change the effect of related parameters. In this study, the values of these coefficients were set to one to account for the complete impact of evaporation and precipitation.

2.2.2 Flux of energy

According to the aerodynamic diffusion equation, the sensible heat flux (H_s), involves the transfer of thermal energy due to the temperature difference between the particles, is calculated as:[39,71,72]

$$H_s = \frac{\rho_{ga} C_a}{r_a}(T_a - T) = \frac{k^2 v_a \varphi}{\left(\ln \frac{z_0}{z_a}\right)^2} \rho_{ga} C_a (T_a - T) \tag{22}$$

where C_a (J/(kg.K)) is the specific heat of the air, T_a and T are the atmospheric and ground temperature, respectively. The convective heat flux (H_c) is computed by considering the internal energy of liquid water, vapour, and air, as:[72]

$$H_c = h_v\left(E + j_w^g\right) + h_{la}\left(P + j_w^l\right) + h_{a0} j_a \tag{23}$$

where h_v, h_{la}, and h_{a0} (J/kg) are the free energy of vapour, liquid water and air, respectively. Therefore, the total energy flux (j_e) can be written as:

$$j_e = k_{rad} R_n + H_s + H_c \tag{24}$$

where k_{rad} (assumed equal to one) is the coefficient that can change the effect of net radiation (R_n). Through the solution of the governing equations for gas flux (j_a) (Eq. (17)), water flux (j_w) (Eq. (21)), and energy flux (j_e) (Eq. (24)), which form the fundamental theoretical framework of soil-atmosphere interaction analysis, valuable insights can be obtained regarding the heterogeneous distribution of heat, water, and gases in the desiccation cracked soils due to permanent climate change.

2.3 Thermo-hydraulic model

The thermo-hydraulic interaction between desiccation cracked soil and the surrounding environment is a complex process involving simultaneous heat and moisture transfer. Heat transfer depends on factors like temperature gradients, thermal conductivity, and radiative heat flux, while moisture transfer is influenced by hydraulic properties like soil-water retention and hydraulic conductivity, along with the presence of cracks as preferential flow pathways. For considering these requirements of a coupled thermo-hydraulic model, the simulations were performed using the CODE_BRIGHT program[53], employing the finite element method. Based on this framework, triangular elements were utilised for spatial discretisation, while the finite difference method was adopted for temporal discretisation. The final geometry of the model and the procedure for determining the model's geometry is explained in Section 3.1.

The material of interest chosen for this investigation is Boom clay, a type of clayey soil that is particularly susceptible to soil desiccation cracking. Boom clay has been extensively the subject of previous studies; hence its thermo-hydraulic parameters have been widely reported.[57-61] As a first initial condition of porous medium, the initial soil temperature is set at 15 °C, based on the research by De Bruyn and Labat[73], where the Boom clay temperature at a depth of 223 m was reported as 16.6 °C. Therefore, a constant soil temperature of 15 °C is assumed as the equilibrium temperature (T_{eq}) of the soil, as the near-surface depths are influenced by temperature fluctuations due to climatic variations. The second initial condition considers an assumed soil porosity of 0.487, falling within the reported range for Boom clay in literature.[57,59,61] Thermo-hydraulic characteristics of Boom clay used in this study are given in Table 1.

One of the critical input parameters for this TH model is climatic data, including temperature, precipitation, relative humidity, wind speed, and radiation. Due to higher rates of drying and susceptibility to cracking in tropical regions, the study area selected for this research is the Qom city. This region is well-known for its high temperatures, prevailing winds, and its vulnerability to subsidence hazards and crack propagation networks.[74] Climatic data corresponding to the study area were collected for a three-year period from 2015 to 2017 as depicted in Fig. 2.

3. Results and discussion

3.1 Statistical analysis of crack geometry and spacing

Understanding the behaviour of cracked soils requires reliable determination of the geometry and spacing of cracks. However, measuring these characteristics in large-scale field studies can be difficult. To overcome this challenge, a statistical approach is employed to make the best use of available dataset in the literature for crack geometries in desiccated soils. This approach enables us to draw valuable insights from limited data and make dependable predictions about crack behaviour under varying conditions. Furthermore, in order to utilise data from small-scale laboratory and numerical studies, a dimensionless parameter called the crack ratio (C_R) has been introduced. This parameter is defined as the ratio of crack width (C_W) to depth (C_D) and is summarised in Table 2 for various studies.

In field-scale studies, crack depth of up to 6 m have been reported[21], and in the study area of this research, deep cracks with considerable lengths have been observed. To cover the full range of crack depths, three values of 1 m, 2.5 m, and 5 m were considered, based on previous researches[21,42] and field observations. According to Table 2, the C_R can vary between 1% and 42%, encompassing a relatively large range. However, selecting only the average value of this range may not be representative of the entire range of C_R. In order to accurately estimate the representative value of the C_R, the variable inference was conducted using RTx software.[75] In Fig. 3(a) the Gaussian and lognormal distributions are plotted alongside the C_R data from Table 2. As observed, the crack width-to-depth ratio follows a lognormal distribution. By utilising the mean and coefficient of variation of the C_R as 13.2 and 85.7%, the probability density function (PDF) for the C_R data was depicted, as shown in Fig. 3(b). The peak of this curve indicates the mode of the data, representing the C_R with the highest density among the available data. Therefore, the first representative value for the C_R was estimated as the mode of the data, which is 5%. The second representative value for the C_R was chosen to be the mean point, being approximately 13% for the data reported in Table 2. To observe the larger C_R effect in this study, the third representative value was estimated using the mean plus twice the standard deviation (i.e., mean + 2σ = 35%). As a result, the three representative points for the C_R have been shown in Fig. 3(b). The modeling scenarios for crack geometry are in accordance with Table 3, where each scenario is named using the format "DiRj". For example, the model D2.5R13 refers to the crack depth of 2.5 m, crack ratio of 13%, and consequently, crack width of 0.325 m.

The spacing between cracks is also of great importance when studying the thermo-hydraulic response of soil to climate change. This is because closely spaced cracks significantly impact the thermo-hydraulic behaviour of soil due to their strong interaction, while widely spaced cracks have a less pronounced effect. In this study, random values for crack spacing were used to cover various crack spacings, assess their effects on soil behaviour, and compare them with the case of intact soil. The crack spacing was defined by two parameters, x and r_i. Parameter x was defined to establish the upper limit of the crack spacing. Based on field observations and the limited geometry of the simulated model, a maximum crack spacing of 10 m was assumed for parameter x. Parameter r_i was introduced to allow for random variation in the crack spacing. This parameter encompasses random values ranging from 0.1 to 1. The product of these two parameters determines the crack spacing ($C_S = x.r_i$). For example, if r_i is set to 0.5, the crack spacing would be 5 m in this case. Based on this definition, the determined range for crack spacing is from 1 m to 10 m. The randomly generated crack spacings are presented in Fig. 4.

The crack geometry and spacing parameters are illustrated schematically in Fig. 5. The final geometry of the model consists of a length of 100 m, representing 14 cracks. According to Fig. 4, the minimum and maximum distances between the cracks are 1.3 m (between 3rd and 4th cracks) and 9.1 m (between 12th and 13th cracks), respectively. The first and last cracks are also positioned approximately 10 m away from the lateral boundaries of the model, ensuring that the lateral boundaries have minimal influence on the behaviour of the cracks. The depth of the soil is considered to be 50 m, covering the range of thermal variations in the soil depth. The geometry of the model and the finite element mesh for model D2.5R13 are illustrated in Fig. 6.

3.2 Soil temperature distribution

The ground temperature determines the availability and accessibility of heat energy. Moreover, cracks, fractures, or fissures in geological formations can act as pathways for heat transfer, altering heat flow patterns. Therefore, in this section, the impact of climatic conditions on the thermal variations of the ground is examined, and results for the cracked and uncracked soil is compared.

3.2.1 Effect of climate change on intact soil

Specific time points were selected based on their distinct temperature characteristics to investigate the impact of climatic conditions on temperature distribution in intact soil. These time points correspond to specific days during the three years of study from 2015 to 2017, including the last day of 2017 (experienced a temperature of 8.75°C), the coldest day in 2016 (-2.8°C), and the warmest day in 2015 (39.1°C). Additionally, three days with an average temperature (20.6 °C) over the three years were chosen.

The temperature distributions for each selected day are presented in Fig. 7. The results indicate that the soil surface temperature is almost equal to the air temperature (T_a) and each soil depth has a different value. The temperature distribution does not show a consistent trend until reaching the equilibrium value of 15 °C (T_{eq}). Fig. 7(a) shows that at the end of 2017, soil temperature increased from 8.6 °C to a maximum of 19 °C at a depth of 4.2 m. Then, the temperature distribution changed until it reached T_{eq} at a depth of 20 m. The distribution of temperature on the coldest day followed the same trend. When the T_a was -2.8 °C, the maximum temperature occurred at a depth of 2.7 m and was equal to 21.2 °C. The opposite trend was observed on the warmest day, where the soil temperature decreased from 38.5 °C to 14.8 °C at a depth of 6.1 m. In other words, when $T_a < T_{eq}$, a soil depth should be expected to have a higher temperature than T_{eq}. On the other hand, when $T_a > T_{eq}$, a soil depth will have a lower temperature than T_{eq}.

Ground temperature is affected by various factors, including soil properties, moisture content, and thermal conductivity. Soil with lower moisture content is more sensitive to temperature changes than moist soil. In general, deeper soil experiences less extreme temperature variations than shallow soil. By delving deeper into the soil, the amplitude of temperature variation diminishes exponentially, primarily influenced by the soil's thermal inertia. Thermal inertia refers to the soil's ability to resist rapid temperature changes. The soil acts as a thermal buffer, absorbing and storing heat during warmer periods and releasing it during cooler periods. This property causes temperature variations to smooth out with increasing depth, as the soil's thermal inertia dampens the impact of external temperature fluctuations. Consequently, the deeper layers of the soil exhibit a more stable temperature profile with reduced thermal fluctuations amplitude. Finally, it should be noted that heat changes in soil can be diverse and non-uniform, particularly when considering average air temperatures.

According to Fig. 7(b), the soil temperature at a depth ranging from 0.9 m to 1.9 m falls between 13.1 °C to 14.2 °C, which is notably lower than the T_{eq}. Of particular interest is the observation of another peak in the thermal distribution during both 2016 and 2017, found at a depth of approximately 7.5 m. Analysing the thermal distribution of 2017, distinct temperature readings were recorded at various depths: 20.6 °C at the soil surface, 14.2 °C at 1.9 m depth, 17 °C at 7.5 m depth, and 15 °C at 25 m depth. These observations indicate a considerable temperature variation within different soil depths during the same time. Furthermore, Fig. 7(b) provides a comprehensive illustration of the relationship between climatic conditions and the equilibrium depth (z_{eq}). Notably, the graph clearly depicts the z_{eq} values for the years 2015, 2016, and 2017, which stand at 7 m, 14 m, and 20 m, respectively. This graphical representation effectively underscores the influence of varying climatic factors on the depth at which thermal equilibrium is attained within the soil profile. These findings are consistent with the research outcomes reported by An et al.[40], Nwankwo and Ogagarue[76], Wang et al.[77], Badache et al.[78].

3.2.2 Effect of cracking and spacing

To investigate the impact of cracks on the soil temperature distribution and make a comparison with intact soil, the D1R5 model was utilised for selected days across three successive years, as depicted in Fig. 8(a). This figure provides a representation of the thermal distribution between the 3rd and 4th cracks, which are spaced 1.3 m apart. The findings indicate that the presence of 1m-depth cracks led to an increase in ground temperature, particularly up to a depth of approximately 2.5 m. Notably, this change resulted in a downward and rightward shift of the curve, ultimately increasing in the minimum temperatures formed in the soil deeper layers. At a depth of 2.5 m, the temperature distribution exhibited an increase of 0.5°C to 1°C due to the presence of cracks. More precisely, the minimum temperature recorded at this depth was 71 cm, 40 cm, and 68 cm deeper than the corresponding point in intact soil for the years 2015, 2016, and 2017, respectively. Furthermore, the minimum temperature at this depth experienced an increase of 0.23°C, 0.36°C, and 0.34°C in those respective years, due to soil cracking. It is important to emphasise that this distribution may vary depending on the depth and spacing of the cracks, as explained in Section 3.2.3.

As the distance between cracks increases, the interaction between them diminishes, and the temperature distribution between the cracks becomes similar to that of the intact soil, as shown in Fig. 8(b). Specifically, the temperature distribution between the 12th and 13th cracks closely matches the thermal distribution observed in the intact soil. However, the behaviour observed near the cracks deviates from the overall trend. When the distance between the cracks decreases, and the air temperature surpasses the soil's equilibrium temperature (e.g., on the warmest day, see Fig. 8(b)), the soil up to a depth of approximately 3.5 m exhibits higher temperatures than the distant cracks. Conversely, when T_a is lower than T_{eq} (e.g., on the coldest day, see Fig. 8(b)), the soil up to a depth of about 3 m demonstrates lower temperatures than the distant cracks. This finding implies that the thermal response of closely-spaced cracked soil is contingent upon the relative difference between the air and the soil equilibrium temperature. For instance, on the warmest day, at a depth of 3 m, the temperature distribution between the 12th and 13th cracks yielded a temperature of 17.5 °C, while between the 3rd and 4th cracks, it reached 19.5 °C, resulting in a temperature difference of 2 °C due to the variation in crack distance. The observations above highlight the complex interplay between crack proximity, air temperature, and thermal behaviour of the soil.

3.2.3 Effect of crack width and depth

The influence of crack width was specifically investigated in models with C_D of 1 m and C_R of 5%, 13%, and 35%, comparing the coldest and warmest days as shown in Fig. 9(a). Since cracks provide preferential pathways for heat and moisture transfer, the crack depth allows for a deeper connection between soil layers and the enclosed crack atmosphere. However, the crack width only has a marginal effect and does not significantly impact the temperature distribution inside the soil, as depicted in Fig. 9(a).

Furthermore, the impact of crack depth was examined by comparing models with C_D of 1 m, 2.5 m, and 5 m, all with the same C_R of 13%, as illustrated in Fig. 9(b). This figure clearly demonstrates that with increasing crack depth under various climatic conditions, z_{eq} also increases. Furthermore, the temperature pattern on the coldest day highlights that maximum temperature are observed at depths of 3 m, 4.4 m, and 7.2 m when the crack depths are 1 m, 2.5 m, and 5 m, respectively. In other words, increasing the crack depth from 1 m to 5 m, results in the maximum temperature occurring 4.2 m deeper. Similarly, on the warmest day, z_{eq} corresponds to depths of 6.4 m, 7.5 m, and 10 m for the crack depths mentioned above. As depicted in the figure, increasing the crack depth reveals greater thermal fluctuations at different depths. For the warmest day, in D1R13, the temperature decreases with a specific gradient until reaching the equilibrium depth. However, in D2.5R13, the temperature decreases from the ground surface to a depth of 0.6 m, followed by a steeper gradient from 0.6 m to 2.5 m, and then continues to decrease with the same gradient as D1R13 from 2.5 m to the equilibrium depth. A similar trend is observed in D5R13, but with the difference that temperature variations persist with a steeper gradient beyond a depth of approximately 0.8 m to 5 m. Thus, in closely spaced cracks, temperature fluctuations intensify with increasing crack depth. These fluctuations can be divided into two parts: the first part corresponds to temperature fluctuations up to the soil depth equal to the crack depth with two different gradients, and the second part extends from the crack depth to the equilibrium depth. These findings also hold true for the coldest days trends.

As depicted in Fig. 8, the temperature distribution between the 12^{th} and 13^{th} cracks for the D1R5 model closely resembles the temperature distribution of intact soil due to reduced interaction. However, as depicted in Fig. 9(c), when the crack depth increases from 1 m to 5 m, it leads to a stronger interaction between the 12^{th} and 13^{th} cracks. Consequently, the temperature distribution between these cracks deviates from the pattern observed in intact soil. Therefore, it can be concluded that as the distance between cracks decreases or the crack depth increases, there is an amplified interaction among the cracks. This results in a distinct temperature pattern within the soil depth, where temperatures lower than T_{eq} experience a greater decrease, while temperatures higher than T_{eq} undergo a greater increase. Indeed, as shown in Fig. 9(c), the temperature trend corresponding to a crack depth of 5 m displays noticeable peaks at depths around 2.5 m and 8 m. These peaks lead to lower temperatures (about 0.7 °C compared to intact soil) at a depth of 2.5 m and higher temperatures (about 0.4 °C compared to intact soil) at a depth of 8 m compared to the trends observed at other crack depths.

3.2.4 Maximum range of temperature variation

The thermal distribution in a specific soil depends on various factors such as climatic conditions, surface cracks geometry, and distance between them, as discussed in Sections 3.2.1, 3.2.2, and 3.2.3. This means that different thermal patterns can be observed for different crack scenarios over the three-year period. It is important to note that every soil depth should experience a limited range of temperature variations under different climate and crack conditions. Therefore, 30 scenarios of the ground thermal distributions are considered, as shown in Fig. 10(a). The results indicate that the temperature distributions among different C_D of 1 m, 2.5 m, and 5 m. It provides a representation of the temperature patterns between the closest cracks and the furthest cracks under varying atmospheric temperatures. The results reveal that all the temperature distributions fall within a certain range, regardless of the crack geometry or climate conditions. This range represents the maximum temperature variations (ΔT) at a specific soil depth.

Considering the Gaussian distribution for the temperature variation in the different soil depths, one can achieve the probability density functions (PDF) as shown in Fig. 10(b) and (c). The results show that, by increasing the soil depth, the average soil temperature decreased from 20°C, at the soil surface to 15°C at a depth of 15 m. Also, the coefficient of variation in the soil temperature decreases from 65% to 1.85% by reaching a depth of 15 m from the ground surface. This leads to a narrower PDF of the soil temperature that shifts towards a lower temperature regime as the soil depth increases. This indicates that the peak of PDF progressively moves from the average air temperature (20.6 °C) towards the equilibrium temperature of the soil (15 °C). Accordingly, it is evident that the uncertainty in the variation of soil temperature decreases by increasing the soil depth, and the average soil temperature tends to a lower temperature. This finding suggests a more stabilised thermal environment with lower temperature fluctuations at greater depths.

Fig. 11 illustrates the lower and upper bounds shown in Fig. 10(a) based on crack depth separately. As the crack depth decreases, the range of maximum temperature fluctuations becomes narrower. Eventually, the minimum range of temperature fluctuations is noticed in the intact soil trends. For example, at a soil depth of 5 m, the maximum temperature variations (ΔT) can extend up to 5 °C, 5.5 °C, 7.6 °C, and 21.9 °C for the intact soil, cracked soil with C_D of 1 m, 2.5 m, and 5 m, respectively. In other words, at a soil depth of 5 m, the temperature fluctuations in the presence of a 5-meter-depth crack are considerably higher, exhibiting an enhanced temperature of 16.9 °C (338%), 16.4 °C (298%), and 14.3 °C (188%) compared to the intact soil, cracked soil with C_D of 1 m, and 2.5 m, respectively. As the equilibrium depth is reached, the range of temperature variations becomes narrower in all cases, eventually converging at a depth close to 20 m.

Fig. 12 provides an estimation of the maximum temperature variation range (ΔT) based on the findings from Fig. 11. It is noted that the influence of crack spacing was taken into account, as the most critical spacing scenarios were considered in Fig. 11. Additionally, the influence of climate change by including different climatic scenarios that align with those depicted in Fig. 11, was incorporated into the results of Fig. 12. Therefore, a comprehensive visualisation of the maximum range of temperature variations (ΔT) at various cracked soil depths is presented in Fig. 12. As depicted in Fig. 12, at the soil surface (Boundary 1, see Fig. 12(b)), ΔT is approximately 42 °C, which indicates the difference between the maximum and minimum air temperatures ($\Delta T_{z=0} = T_{a,max} - T_{a,min}$) experienced by the ground over time. Notably, this value is independent of the crack depth. Moving towards deeper soil layers, variations in ΔT are strongly influenced by crack depth. According to Fig. 12(b), boundary 3, indicates ΔT changes for a crack depth of 1 m, demonstrates a uniformly decreasing pattern. However, boundary 2, representing ΔT variations for a crack depth of 5 m, exhibits non-uniform changes influenced by different decreasing slopes. Moreover, ΔT variations at a soil depth of 10 m (Boundary 4) exhibit an ascending slope from a crack depth of 1 m to 5 m. This outcome suggests that, a wider temperature fluctuation range is encompassed with an increasing crack depth at a soil depth of 10 m.

Fig. 13(a) clearly shows the decreasing rate of ΔT in deeper cracked soil layers. According to the results, the soil with a 1-meter crack depth exhibits the highest ΔT decreasing rate with increasing soil depth, while the soil with a 5-meter crack depth shows the lowest decreasing rate. For example, at a depth of 1 m below the ground surface, the corresponding ΔT for crack depths of 1 m, 2.5 m, and 5 m are 25 °C, 27.2 °C, and 33 °C, respectively. In other words, ΔT for a soil with 5 m crack depth is 33% and 21.3% higher than that of 1 and 2.5 m crack depths, respectively (as Fig. 13(b)). However, at 4 m soil depth, ΔT for a soil with 5 m crack depth is 264% and 150% higher than for 1 m and 2.5 m crack depths, respectively. As shown in Fig. 13(b), this difference reaches its maximum value at 5 m below the ground surface (298.2% and 187.5%). Beyond this depth, the difference gradually decreases, suggesting that it tends to approach zero at the equilibrium depth. In other terms, it is demonstrated in Fig. 13(b) that for each soil depth, ΔT corresponds to D5R13, how much percentage is higher than ΔT corresponds to D1R13 and D2.5R13.

Predicting the maximum temperature variations (ΔT) at a specific intact soil depth is relatively simpler. As shown in Fig. 14, the trend of ΔT for intact soil depends solely on the soil depth and follows an exponential trend. By fitting the available data, the relationship can be expressed as:

$$\Delta T = 23.2708\,\exp[-0.30381z] \tag{25}$$

where z is the soil depth. Additionally, this equation can approximate the equilibrium depth at which $\Delta T = 0$. This equilibrium depth in recent studies has been reported to be approximately 15 m.[76,78] The proposed equation for temperature variations at a soil depth of 15 m yielded a negligible result of 0.24 °C, which is consistent with recent studies.

3.3 Soil saturation distribution

The ground surface experiences substantial hydraulic fluctuations in response to seasonal climatic changes, leading to variations in soil moisture content, infiltration rates, and so on. On rainy days, infiltration occurs, leading to saturation of the shallow soil layer and runoff formation in heavy rainfall conditions. On the other hand, cracks facilitate water penetration to deeper soil layers. However, during those days with intense radiation and high temperatures, the ground surface suffers evaporation much more severe. Evaporation occurs at different rates from the soil surface and crack walls. Therefore, in the vicinity of cracks, there are more pronounced changes in the flow regime. In this section, the variation of soil saturation degree (S_r) and the influence of different crack geometries and spacing will be examined.

3.3.1 Effect of crack width

The two-dimensional distribution of soil saturation degree (S_r) in cracked soil at the end of 2017 is compared based on the crack width, as shown in Fig. 15. This distribution is influenced by various factors such as the history of hydraulic loading (seasonal changes in climatic conditions) and soil hydraulic parameters. Therefore, the chosen timeframe specifically addresses the impact of crack width on the extent of soil desiccation. According to this figure, desiccation is more severe in the cracked regions. Moreover, this intensity becomes more pronounced with decreasing distance between cracks. The distribution of saturation degree in all three cases indicates that cracks intensify the soil drying along the vertical direction. This is evident from the downward deflection of contour lines towards the cracks and their upward inclination as they move away from the cracks. As a result, this leads to heterogeneous moisture variations at different soil depths, unlike the case of intact soil with a homogeneous moisture distribution along the horizon. On the other hand, in closely spaced cracks, narrower cracks demonstrate higher surface desiccation. As observed, the contour line between two cracks in Fig. 15(a) represents a value of 23.3%, while the same point in Fig. 15(c) represents a value of 30%. Furthermore, comparing the contour lines between the two cracks in this figure reveals that the contour lines tilt upwards with an increase in crack width, indicating less drying in wider cracks. The observed results are consistent with field observations and laboratory experiments findings reported by Adam and Hanks[41], Ritchie and Adam[42], Poulsen[45].

3.3.2 Effect of crack depth and spacing

For a more detailed examination of the impact of crack parameters, with a focus on crack depth and distance, the degree of soil saturation was considered as a measure of soil dryness for different distances from the 3rd crack, as depicted in the schematic diagram of Fig. 16(d). The degree of saturation was determined up to a distance of 60 cm from the 3rd crack aperture, with intervals of 10 cm. The comparison between Fig. 16(a) and (b) reveals the influence of different periods on the degree of soil dryness due to seasonal climate changes. Since homogeneous and isotropic soil has a uniform moisture distribution, the degree of saturation remains constant at a specific depth within the soil. However, in cracked soil, the degree of saturation at a constant depth depends on the distance from the crack.

Fig. 16(a) demonstrates that at the end of 2015 (after one year), the overall intact soil surface dryness is higher compared to the cracked soil (less S_r). The cracked soil within a distance of 60 cm from the crack, reaches its minimum level of dryness (maximum saturation degree), indicating approximately 4.5% higher S_r compared to the intact soil. Additionally, in the regions closer to the crack especially at a distance of 20 cm, the soil dryness is higher in crack ratios of 5% and 13% (D1R5 and D1R13) compared to other cases. Among all the cases of cracked soil, the surface soil dryness was highest in D1R5, and with increasing crack depth and width, less surface dryness was observed.

After three years, at the end of 2017, the cracked soil generally exhibited higher ground surface dryness compared to the intact soil, as shown in Fig. 16(b). By comparing the two different periods, it is evident that during this time, S_r in the intact soil decreased from 31% to 22.5%, indicating an 8.5% reduction. On the other hand, S_r in the cracked soil at a distance of 60 cm from the crack decreased from approximately 35.5% to 23.3%, indicating a 12.2% reduction. Therefore, it can be concluded that over time, despite climate fluctuations involving rainfalls, various wind velocity, relative humidity, radiation, and temperatures, the cracked soil exhibits a higher rate of ground surface drying compared to intact soil.

Among the cases of cracked soil, at a distance of 30 cm, S_r in D1R5 decreased from 31.8% to 21.9% after two years, indicating a 9.9% reduction. Similarly, S_r in D2.5R13 decreased from 34% to 22%, indicating a 12% reduction. Hence, it can be inferred from the results that among the different crack scenarios, deeper cracks experience a higher rate of drying. Furthermore, the results demonstrate that the maximum dryness at the ground surface occurs at a specific distance from the crack aperture, which was obtained to be 20 cm in this study.

It is important to mention that the moisture distribution difference between intact and cracked soil is not limited to surface dryness. Cracks also lead to significant drying of the considerable soil depth, which is consistent with the results shown in Fig. 15. Therefore, to investigate the impact of cracks on deeper soil drying, the same diagrams were plotted for a depth of 1 m below the ground surface, as shown in Fig. 16(c). According to the results, the drying at a depth of 1 m in cracked soil is obviously greater than intact soil, which is more significant near the crack walls. Among the crack scenarios, D2.5R13 consistently showed a 5% lower degree of saturation than D1R5, D1R13, and D1R35 at all distances from the crack wall. However, the crack ratio did not impact the soil depth drying, and all crack scenarios with a crack depth of 1 m matched each other. In 60 cm and zero distance, corresponding to the crack wall, the soil saturation in D2.5R13 was 10% and 37.5% lower than intact soil, respectively. Therefore, it can be concluded that the increased drying in cracked soils is mainly due to the intensity of crack effects on moisture redistribution at deeper soil levels.

Conclusions

The focus of this study was on the thermo-hydraulic analysis of cracked soil to investigate the temperature and moisture dynamics, under the soil-atmosphere interaction. The governing equations for unsaturated porous media, including balance and constitutive equations, and those governing soil-atmosphere interaction, were incorporated into a coupled TH formulation. Advective and non-advective fluxes were calculated using Darcy and Fick's law, respectively, to account for water and gas flow, as well as water vapour diffusion. Additionally, heat transfer through the porous medium was considered using Fourier's law and implemented in the CODE_BRIGHT finite element program. In order to utilise the full range of crack geometry data reported from large-scale field studies, small-scale laboratory experiments, and numerical simulations, a dimensionless parameter, crack ratio (C_R), was defined. Based on statistical analysis using the RTx software, the best distribution for the reported crack geometries from several studies was found to be lognormal. Different geometries were selected to cover the entire range of data. Afterwards, crack scenarios were implemented in the numerical model.

Meteorological data for Qom city, considered as one of the most prone areas to subsidence in Iran, were obtained for the years 2015 to 2017 and used as input for the numerical model. Boom clay was chosen as the geomaterial for numerical model which is well-justified due to its geotechnical relevance, extensive data availability, and practical applications. Boom clay's unique properties, especially its high sensitivity to desiccation, make it a suitable choice for investigating the complex thermo-hydraulic behaviour of cracked soils. Finally, numerical computations were performed to investigate the interaction between cracked soil and atmosphere, and its impact on temperature and moisture dynamics in the soil. Based on the results, some key conclusions can be drawn as follows:

(1) Ground temperature fluctuations induced by climate changes are particularly significant in shallow soil depths (up to about 20 m), and their magnitude depends on soil properties as well as the depth and spacing of cracks. The findings demonstrate that when the air temperature is lower than the equilibrium temperature ($T_a < T_{eq}$), the temperature at a certain soil depth is expected to be higher than T_{eq}. Conversely, when $T_a > T_{eq}$, the temperature at that soil depth will be lower than T_{eq}. This suggests that while the soil is subjected to climatic conditions, the deeper ground temperature is predominantly influenced by history of the thermo-hydraulic loading rather than instantaneous climate variations.

(2) The results showed that a specific region can be identified for temperature variations in the ground, where the temperature profile pattern under any climatic conditions and crack scenarios is necessarily bounded to that region. Thus, significant temperature variations can be expected and estimated at evey soil depth. In this study, the range of temperature variations was determined for each soil depth and classified based on the crack depth. It should be noted that these are maximum values simulated for the most critical scenarios. Finally, for cracked soil, a surface was defined to estimate the ΔT in

the ground up to a depth of 10 m. Additionally, for intact soil, a relationship was proposed to estimate ΔT for each soil depth.

(3) Statistical analyses highlighted considerable uncertainty in surface soil temperature due to its sensitivity to climatic changes and surface cracks. However, as the soil depth increases, the uncertainty in temperature variation decreases, and the average soil temperature approaches an equilibrium value.

(4) Lastly, the impact of different crack scenarios on soil desiccation due to climatic variations was investigated. A two-dimensional distribution of the degree of saturation was presented to examine the influence of crack width on surface and deeper soil desiccation. The results showed that over time, cracked soil exhibited about 1.4 times higher rates of desiccation than uncracked soil. Among the crack scenarios, deeper cracks demonstrated more severe desiccation rates, about 1.2 times higher, because they lead to the desiccation of a greater depth of soil.

Acknowledgements

The authors wish to acknowledge the support of the European Commission via a Marie Curie Fellowship awarded to Dr. Saeed Tourchi through the research grant SLOPETEMP (Grant agreement ID:101033084).

References

1. Wang D, Lu L, Zhang W, Cui P. Numerical and analytical analysis of groundwater influence on the pile geothermal heat exchanger with cast-in spiral coils. Applied energy. 2015;160:705-14. https://doi.org/10.1016/j.apenergy.2015.04.037
2. Lou Y, Fang PF, Xie XY, Chong CS, Li FY, Liu CY, Wang ZJ, Zhu DY. Numerical research on thermal response for geothermal energy pile groups under groundwater

flow. Geomechanics for Energy and the Environment. 2021;28:100257. https://doi.org/10.1016/j.gete.2021.100257

3. Fuentes R, Pinyol N, Alonso E. Effect of temperature induced excess porewater pressures on the shaft bearing capacity of geothermal piles. Geomechanics for Energy and the Environment. 2016;8:30-7. https://doi.org/10.1016/j.gete.2016.10.003
4. Guo Y, Zhang G, Liu S. Investigation on the thermal response of full-scale PHC energy pile and ground temperature in multi-layer strata. Applied Thermal Engineering. 2018;143:836-48. https://doi.org/10.1016/j.applthermaleng.2018.08.005
5. Faizal M, Bouazza A, McCartney JS, Haberfield C. Effects of cyclic temperature variations on thermal response of an energy pile under a residential building. Journal of Geotechnical and Geoenvironmental Engineering. 2019;145(10):04019066. https://doi.org/10.1061/(ASCE)GT.1943-5606.0002147
6. Laloui L, Sutman M. Experimental investigation of energy piles: From laboratory to field testing. Geomechanics for Energy and the Environment. 2021;27:100214. https://doi.org/10.1016/j.gete.2020.100214
7. Loria AF, Ravera E, Laloui L. Thermo-hydro-mechanical behavior of energy barrettes: Field experiments and numerical simulations. Geomechanics for Energy and the Environment. 2023;34:100451. https://doi.org/10.1016/j.gete.2023.100451
8. Radioti G, Sartor K, Charlier R, Dewallef P, Nguyen F. Effect of undisturbed ground temperature on the design of closed-loop geothermal systems: A case study in a semi-urban environment. Applied Energy. 2017;200:89-105. https://doi.org/10.1016/j.apenergy.2017.05.070
9. Dahl MB, Priemé A, Brejnrod A, Brusvang P, Lund M, Nymand J, Kramshøj M, Ro-Poulsen H, Haugwitz MS. Warming, shading and a moth outbreak reduce tundra

carbon sink strength dramatically by changing plant cover and soil microbial activity. Scientific Reports. 2017;7(1):16035. https://doi.org/10.1038/s41598-017-16007-y

10. Farooq M, Nazir A, Anjum S, Farooq B, Yousuf S. Soil Microbial Biochemical Activity and Influence of Climate Change. InClimate Change and Microbiome Dynamics. 2023;137-155. https://doi.org/10.1007/978-3-031-21079-2_10

11. Hernández-Lara A, Ros M, Cuartero J, Vivo JM, Lozano-Pastor P, Pascual JA. Effects of solarisation combined with compost on soil pathogens and the microbial community in a spinach cropping system. Agriculture, Ecosystems & Environment. 2023;346:108359. https://doi.org/10.1016/j.agee.2023.108359

12. Davidson EA, Janssens IA. Temperature sensitivity of soil carbon decomposition and feedbacks to climate change. Nature. 2006;440(7081):165-73. https://doi.org/10.1038/nature04514

13. Shi BX, Chen SS, Han HQ, Zheng CF. Expansive soil crack depth under cumulative damage. The Scientific World Journal. 2014;2014. https://doi.org/10.1155/2014/498437

14. Zhang C, Lu N. Unitary definition of matric suction. Journal of Geotechnical and Geoenvironmental Engineering. 2019;145(2):02818004. https://doi.org/10.1061/(ASCE)GT.1943-5606.0002004

15. Pouya A, Vo TD, Hemmati S, Tang AM. Modeling soil desiccation cracking by analytical and numerical approaches. International Journal for Numerical and Analytical Methods in Geomechanics. 2019;43(3):738-63. https://doi.org/10.1002/nag.2887

16. Tang CS, Zhu C, Cheng Q, Zeng H, Xu JJ, Tian BG, Shi B. Desiccation cracking of soils: A review of investigation approaches, underlying mechanisms, and influencing

factors. Earth-Science Reviews. 2021;216:103586. https://doi.org/10.1016/j.earscirev.2021.103586

17. Rodríguez R, Sanchez M, Ledesma A, Lloret A. Experimental and numerical analysis of desiccation of a mining waste. Canadian Geotechnical Journal. 2007;44(6):644-58. https://doi.org/10.1139/t07-016
18. Yin P, Vanapalli SK, Yu S. Morphological characteristics of desiccation-induced cracks in cohesive soils: a critical review. Bulletin of Engineering Geology and the Environment. 2022;81(12):503. https://doi.org/10.1007/s10064-022-03003-4
19. Tang CS, Cui YJ, Tang AM, Shi B. Experiment evidence on the temperature dependence of desiccation cracking behaviour of clayey soils. Engineering Geology. 2010;114(3-4):261-6. https://doi.org/10.1016/j.enggeo.2010.05.003
20. Luo Y, Zhang J, Zhou Z, Victor C. Modelling preferential flow induced by dynamic changes of desiccation cracks: A comparative numerical study. Geoderma. 2023;433:116471. https://doi.org/10.1016/j.geoderma.2023.116471
21. Morris PH, Graham J, Williams DJ. Cracking in drying soils. Canadian Geotechnical Journal. 1992;29(2):263-77. https://doi.org/10.1139/t92-030
22. Konrad JM, Ayad R. Desiccation of a sensitive clay: field experimental observations. Canadian Geotechnical Journal. 1997;34(6):929-42. https://doi.org/10.1139/t97-063
23. Philip LK, Shimell H, Hewitt PJ, Ellard HT. A field-based test cell examining clay desiccation in landfill liners. Quarterly Journal of Engineering Geology and Hydrogeology. 2002;35(4):345-54. https://doi.org/10.1144/1470-9236/2001-37
24. Yu Z, Eminue OO, Stirling R, Davie C, Glendinning S. Desiccation cracking at field scale on a vegetated infrastructure embankment. Géotechnique Letters. 2021;11(1):88-95. https://doi.org/10.1680/jgele.20.00108

25. Miller CJ, Mi H, Yesiller N. Experimental analysis of desiccation crack propagation in clay liners 1. JAWRA Journal of the American Water Resources Association. 1998;34(3):677-86. https://doi.org/10.1111/j.1752-1688.1998.tb00964.x
26. Wang LL, Tang CS, Shi B, Cui YJ, Zhang GQ, Hilary I. Nucleation and propagation mechanisms of soil desiccation cracks. Engineering Geology. 2018;238:27-35. https://doi.org/10.1016/j.enggeo.2018.03.004
27. Ferreira SR, Araújo AG, Barbosa FA, Silva TC, Bezerra IM. Analysis of changes in volume and propagation of cracks in expansive soil due to changes in water content. Revista Brasileira de Ciência do Solo. 2020;44. https://doi.org/10.36783/18069657rbcs20190169
28. Tang CS, Cheng Q, Leng T, Shi B, Zeng H, Inyang HI. Effects of wetting-drying cycles and desiccation cracks on mechanical behaviour of an unsaturated soil. Catena. 2020;194:104721. https://doi.org/10.1016/j.catena.2020.104721
29. Zeng H, Tang CS, Zhu C, Vahedifard F, Cheng Q, Shi B. Desiccation cracking of soil subjected to different environmental relative humidity conditions. Engineering Geology. 2022;297:106536. https://doi.org/10.1016/j.enggeo.2022.106536
30. Tian BG, Cheng Q, Tang CS, Shi B. Healing behaviour of desiccation cracks in a clayey soil subjected to different wetting rates. Engineering Geology. 2023;313:106973. https://doi.org/10.1016/j.enggeo.2022.106973
31. Amarasiri AL, Kodikara JK. Numerical modelling of a field desiccation test. Géotechnique. 2013;63(11):983-6. https://doi.org/10.1680/geot.12.P.010
32. Sánchez M, Manzoli OL, Guimarães LJ. Modeling 3-D desiccation soil crack networks using a mesh fragmentation technique. Computers and Geotechnics. 2014;62:27-39. https://doi.org/10.1016/j.compgeo.2014.06.009

33. Stirling RA, Glendinning S, Davie CT. Modelling the deterioration of the near surface caused by drying induced cracking. Applied Clay Science. 2017;146:176-85. https://doi.org/10.1016/j.clay.2017.06.003
34. Levatti HU, Prat PC, Ledesma A. Numerical and experimental study of initiation and propagation of desiccation cracks in clayey soils. Computers and Geotechnics. 2019;105:155-67. https://doi.org/10.1016/j.compgeo.2018.09.015
35. Houcem T, Alassaf Y, Jamei M, Olivella S. Desiccation cracks prediction using a 3D finite elements model. International Journal of Geotechnical Engineering. 2023:1-5. https://doi.org/10.1080/19386362.2023.2202595
36. Guo L, Chen G, Ding L, Zheng L, Gao J. Numerical simulation of full desiccation process of clayey soils using an extended DDA model with soil suction consideration. Computers and Geotechnics. 2023;153:105107. https://doi.org/10.1016/j.compgeo.2022.105107
37. Blight GE. Interactions between the atmosphere and the earth. Géotechnique. 1997;47(4):715-67. https://doi.org/10.1680/geot.1997.47.4.713
38. Gens A. Soil–environment interactions in geotechnical engineering. Géotechnique. 2010;60(1):3-74. https://doi.org/10.1680/geot.9.P.109
39. Hemmati S, Gatmiri B, Cui YJ, Vincent M. Thermo-hydro-mechanical modelling of soil settlements induced by soil-vegetation-atmosphere interactions. Engineering Geology. 2012;139:1-6. https://doi.org/10.1016/j.enggeo.2012.04.003
40. An N, Hemmati S, Cui Y. Numerical analysis of soil volumetric water content and temperature variations in an embankment due to soil-atmosphere interaction. Computers and Geotechnics. 2017;83:40-51. https://doi.org/10.1016/j.compgeo.2016.10.010

41. Adams JE, Hanks RJ. Evaporation from soil shrinkage cracks. Soil Science Society of America Journal. 1964;28(2):281-4. https://doi.org/10.2136/sssaj1964.03615995002800020043x
42. Ritchie JT, Adams JE. Field measurement of evaporation from soil shrinkage cracks. Soil Science Society of America Journal. 1974;38(1):131-4. https://doi.org/10.2136/sssaj1974.03615995003800010040x
43. Hatano R, Nakamoto H, Sakuma T, Okajima H. Evapotranspiration in cracked clay field soil. Soil Science and Plant Nutrition. 1988;34(4):547-55. https://doi.org/10.1080/00380768.1988.10416470
44. Poulsen TG, Cai W, Garg A. Water evaporation from cracked soil under moist conditions as related to crack properties and near-surface wind speed. European Journal of Soil Science. 2020;71(4):627-40. https://doi.org/10.1111/ejss.12926
45. Poulsen TG. Predicting evaporation from moist, cracked soil, based on near-surface wind speed, crack width and crack distance. European Journal of Soil Science. 2022;73(1):e13215. https://doi.org/10.1111/ejss.13215
46. Cuadrado A, Najdi A, Ledesma A, Olivella S, Prat PC. THM analysis of a soil drying test in an environmental chamber: The role of boundary conditions. Computers and Geotechnics. 2022;141:104495. https://doi.org/10.1016/j.compgeo.2021.104495
47. Adams JE, Ritchie JT, Burnett E, Fryrear DW. Evaporation from a simulated soil shrinkage crack. Soil Science Society of America Journal. 1969;33(4):609-13. https://doi.org/10.2136/sssaj1969.03615995003300040034x
48. Selim HM, Kirkham D. Soil temperature and water content changes during drying as influenced by cracks: A laboratory experiment. Soil Science Society of America Journal. 1970;34(4):565-9. https://doi.org/10.2136/sssaj1970.03615995003400040010x

49. Tong F, Jing L, Zimmerman RW. An effective thermal conductivity model of geological porous media for coupled thermo-hydro-mechanical systems with multiphase flow. International Journal of Rock Mechanics and Mining Sciences. 2009;46(8):1358-69. https://doi.org/10.1016/j.ijrmms.2009.04.010
50. Du C, Yu J, Wang P, Zhang Y. Analysing the mechanisms of soil water and vapour transport in the desert vadose zone of the extremely arid region of northern China. Journal of Hydrology. 2018;558:592-606. https://doi.org/10.1016/j.jhydrol.2017.09.054
51. Wen W, Lai Y, You Z. Numerical modeling of water–heat–vapor–salt transport in unsaturated soil under evaporation. International Journal of Heat and Mass Transfer. 2020;159:120114. https://doi.org/10.1016/j.ijheatmasstransfer.2020.120114
52. Panday S, Corapcioglu MY. Reservoir transport equations by compositional approach. Transport in Porous Media. 1989;4:369-93. https://doi.org/10.1007/BF00165780
53. Olivella S, Gens A, Carrera J, Alonso EE. Numerical formulation for a simulator (CODE_BRIGHT) for the coupled analysis of saline media. Engineering computations. 1996;13(7):87-112. https://doi.org/10.1108/02644409610151575
54. Olivella S, Carrera J, Gens A, Alonso EE. Nonisothermal multiphase flow of brine and gas through saline media. Transport in porous media. 1994;15:271-93. https://doi.org/10.1007/BF00613282
55. Fredlund DG, Rahardjo H. Soil mechanics for unsaturated soils. United Kingdom: Wiley, 1993.
56. Gens A, Olivella S. THM phenomena in saturated and unsaturated porous media: Fundamentals and formulation. Revue française de génie civil. 2001;5(6):693-717. https://doi.org/10.1080/12795119.2001.9692323

57. Delage P, Sultan N, Cui YJ. On the thermal consolidation of Boom clay. Canadian Geotechnical Journal. 2000;37(2):343-54. https://doi.org/10.1139/t99-105

58. Dehandschutter B, Vandycke S, Sintubin M, Vandenberghe N, Wouters L. Brittle fractures and ductile shear bands in argillaceous sediments: inferences from Oligocene Boom Clay (Belgium). Journal of Structural Geology. 2005;27(6):1095-112. https://doi.org/10.1016/j.jsg.2004.08.014

59. Gens A, Vaunat J, Garitte B, Wileveau Y. In situ behaviour of a stiff layered clay subject to thermal loading: observations and interpretation. InStiff Sedimentary Clays: Genesis and Engineering Behaviour: Géotechnique Symposium in Print. 2007;123-144. https://doi.org/10.1680/ssc.41080.0011

60. François B, Laloui L, Laurent C. Thermo-hydro-mechanical simulation of ATLAS in situ large scale test in Boom Clay. Computers and Geotechnics. 2009;36(4):626-40. https://doi.org/10.1016/j.compgeo.2008.09.004

61. Bernier F, Li XL, Bastiaens W. Twenty-five years' geotechnical observation and testing in the Tertiary Boom Clay format. InStiff Sedimentary Clays: Genesis and Engineering Behaviour: Géotechnique Symposium in Print. 2007;223-231. https://doi.org/10.1680/ssc.41080.0020

62. van Genuchten MT. A closed-form equation for predicting the hydraulic conductivity of unsaturated soils. Soil science society of America journal. 1980;44(5):892-8. https://doi.org/10.2136/sssaj1980.03615995004400050002x

63. Mualem Y. A new model for predicting the hydraulic conductivity of unsaturated porous media. Water resources research. 1976;12(3):513-22. https://doi.org/10.1029/WR012i003p00513

64. Sadeghi H, Nasiri H. Hysteresis of soil water retention and shrinkage behaviour for various salt concentrations. Géotechnique Letters. 2021;11(1):21-9. https://doi.org/10.1680/jgele.20.00047

65. Hedayati-Azar A, Sadeghi H. Semi-empirical modelling of hydraulic conductivity of clayey soils exposed to deionized and saline environments. Journal of Contaminant Hydrology. 2022;249:104042. https://doi.org/10.1016/j.jconhyd.2022.104042

66. Darzi AG, Sadeghi H, Zhou C. A soil-brine retention model for wetting processes considering the hysteresis effects. Transportation Geotechnics. 2023;41:101032. https://doi.org/10.1016/j.trgeo.2023.101032

67. Delahaye CH, Alonso EE. Soil heterogeneity and preferential paths for gas migration. Engineering geology. 2002;64(2-3):251-71. https://doi.org/10.1016/S0013-7952(01)00104-1

68. Bear J, Bensabat J, Nir A. Heat and mass transfer in unsaturated porous media at a hot boundary: I. One-dimensional analytical model. Transport in porous media. 1991;6:281-98. https://doi.org/10.1007/BF00208954

69. Volckaert G, Bernier F, Alonso E, Gens A, Samper J, Villar M, Martin-Martin PL, Cuevas J, Campos R, Thomas H, Imbert C. Thermal-hydraulic-mechanical and geochemical behaviour of the clay barrier in radioactive waste repositories (model development and validation). EUR(Luxembourg) 1996.

70. Sellers PJ, Mintz YC, Sud YE, Dalcher A. A simple biosphere model (SiB) for use within general circulation models. Journal of the atmospheric sciences. 1986;43(6):505-31. https://doi.org/10.1175/1520-0469(1986)043<0505:ASBMFU>2.0.CO;2

71. Noilhan J, Planton S. A simple parameterization of land surface processes for meteorological models. Monthly weather review. 1989;117(3):536-49. https://doi.org/10.1175/1520-0493(1989)117<0536:ASPOLS>2.0.CO;2
72. Samat S. Thermomechanical modelling of ground response under environmental actions. Universitat Politècnica de Catalunya 2016.
73. De Bruyn D, Labat S. The second phase of ATLAS: the continuation of a running THM test in the HADES underground research facility at Mol. Engineering Geology. 2002;64(2-3):309-16. https://doi.org/10.1016/S0013-7952(01)00109-0
74. Sadeghi H, Darzi AG, Voosoghi B, Garakani AA, Ghorbani Z, Mojtahedi SF. Assessing the vulnerability of Iran to subsidence hazard using a hierarchical FUCOM-GIS framework. Remote Sensing Applications: Society and Environment. 2023;31:100989. https://doi.org/10.1016/j.rsase.2023.100989
75. Mahsuli M, Haukaas T. Computer program for multimodel reliability and optimization analysis. Journal of computing in civil engineering. 2013;27(1):87-98. https://doi.org/10.1061/(ASCE)CP.1943-5487.0000204
76. Nwankwo C, Ogagarue D. An investigation of temperature variation at soil depths in parts of Southern Nigeria. American journal of environmental engineering. 2012;2(4):142-7. https://doi.org/10.5923/j.ajee.20120205.05
77. Wang CL, Liu HL, Kong GQ, Ng CW, Wu D. Model tests of energy piles with and without a vertical load. Environmental Geotechnics. 2016;3(4):203-13. https://doi.org/10.1680/jenge.15.00020
78. Badache M, Eslami-Nejad P, Ouzzane M, Aidoun Z, Lamarche L. A new modeling approach for improved ground temperature profile determination. Renewable Energy. 2016;85:436-44. https://doi.org/10.1016/j.renene.2015.06.020

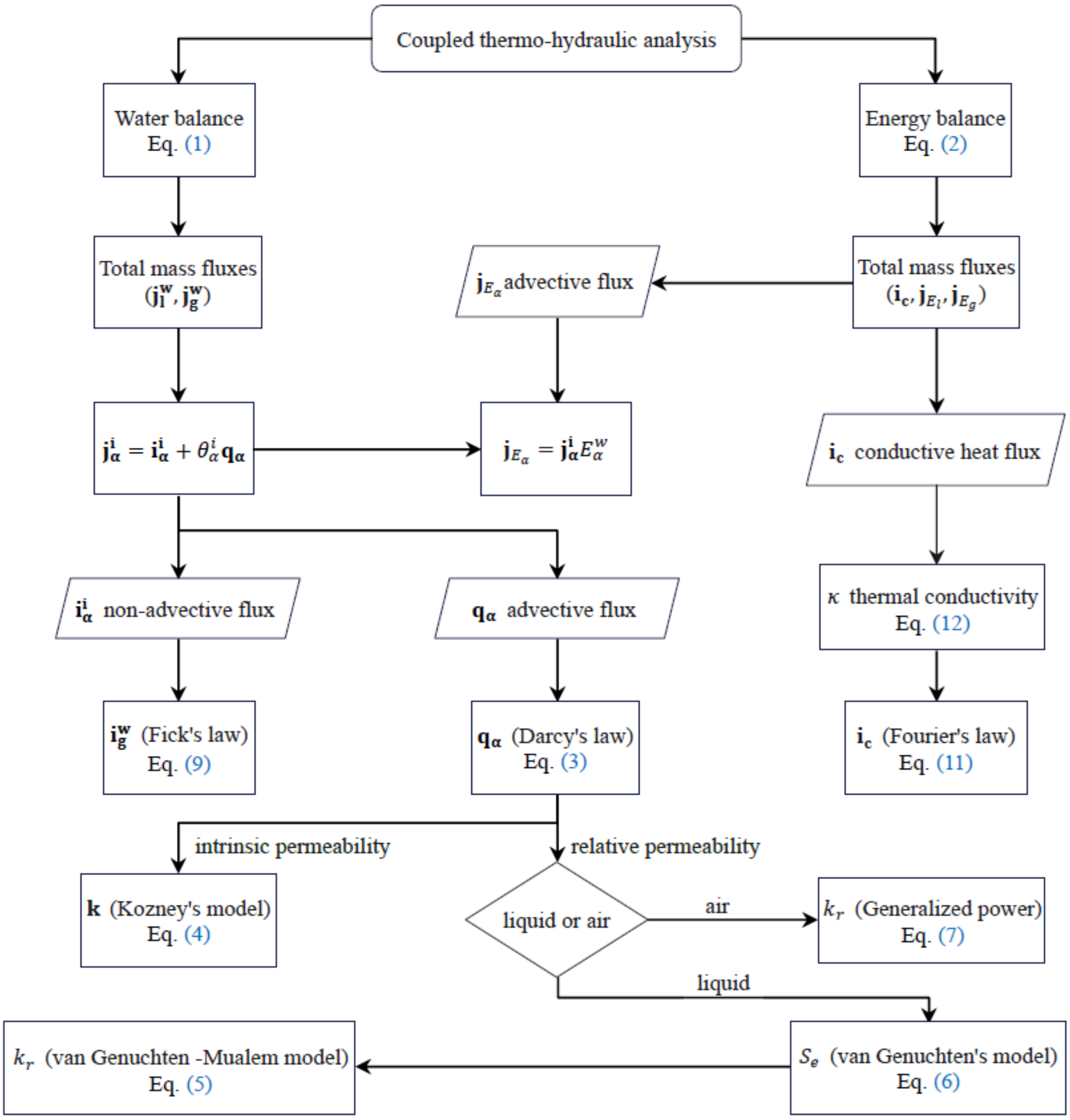

Fig. 1. Flowchart of the relation between balance and constitutive equations.

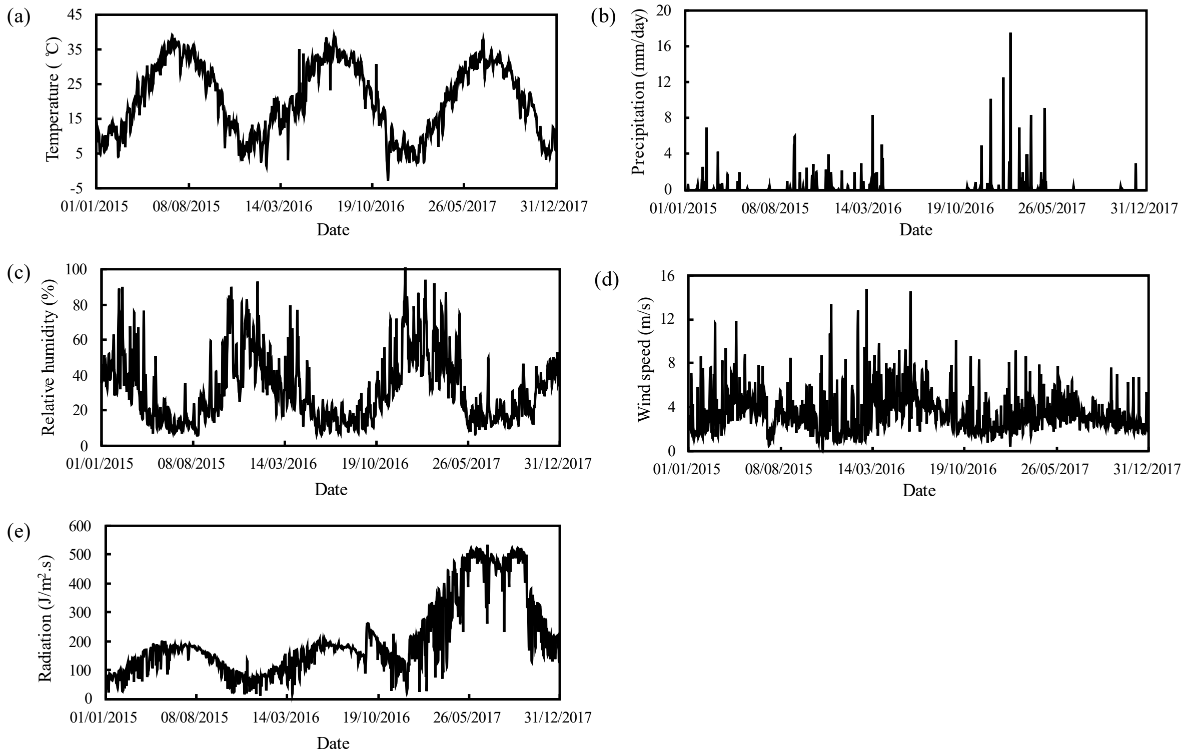

Fig. 2. Climate data for Qom city, (a) temperature, (b) precipitation, (c) relative humidity, (d) wind speed, (e) radiation.

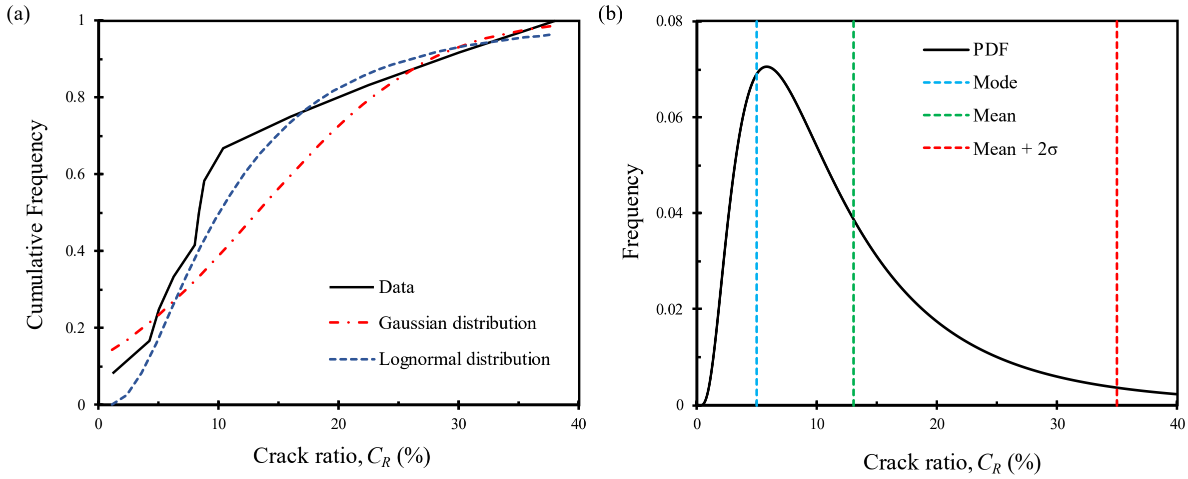

Fig. 3. (a) Gaussian and lognormal distributions and (b) PDF of the crack ratio data.

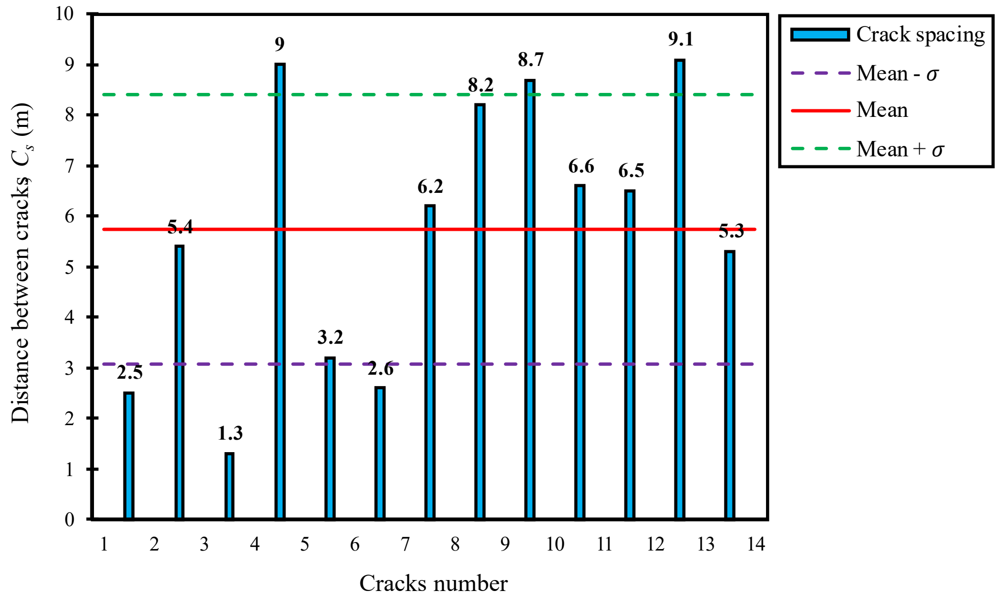

Fig. 4. Randomly generated crack spacing.

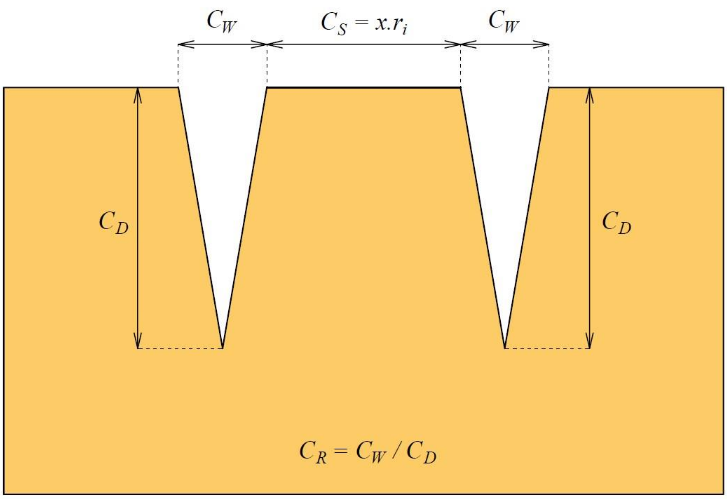

Fig. 5. Schematic diagram of the crack geometry and spacing.

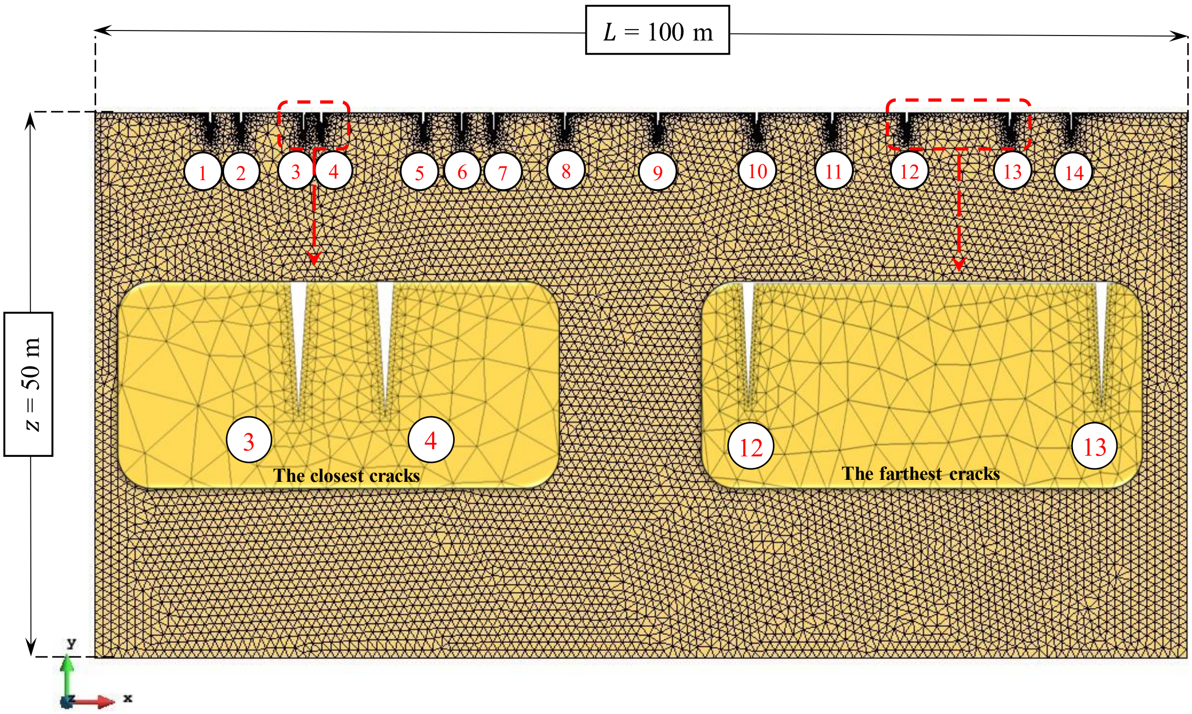

Fig. 6. Model geometry and finite element mesh for model D2.5R13 (Table 3).

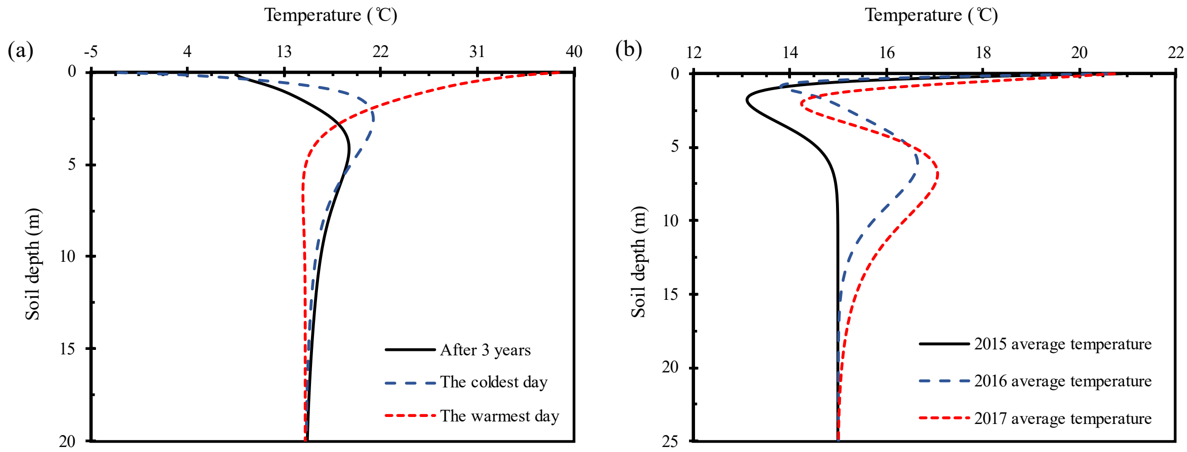

Fig. 7. Effects of climate change on the temperature distribution in the intact soil.

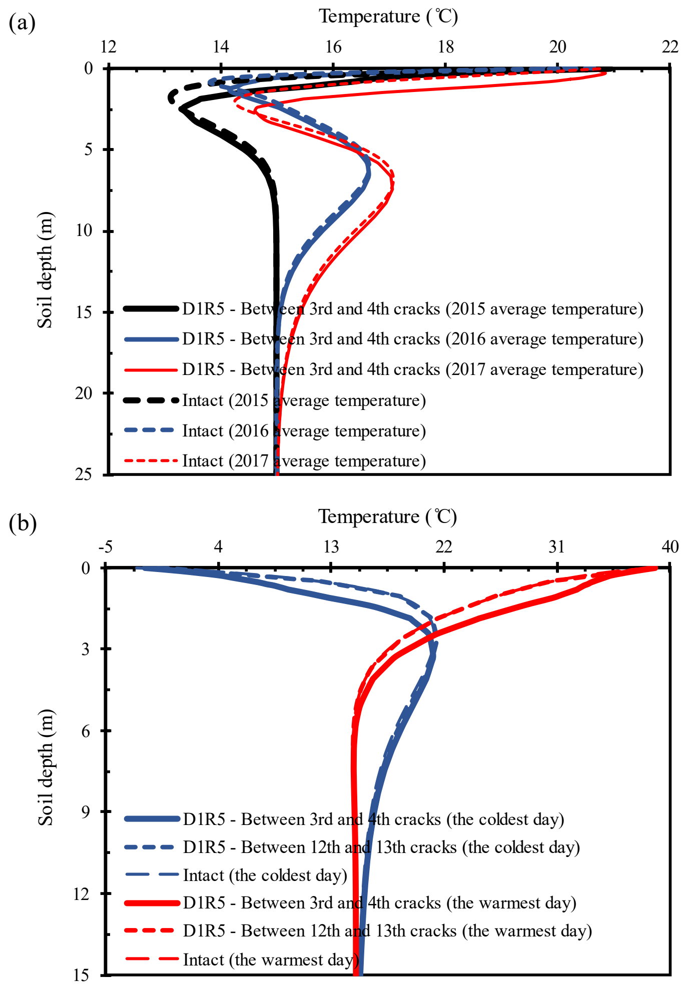

Fig. 8. (a) Comparison of the cracked and intact soil and (b) effect of the crack spacing on temperature distribution.

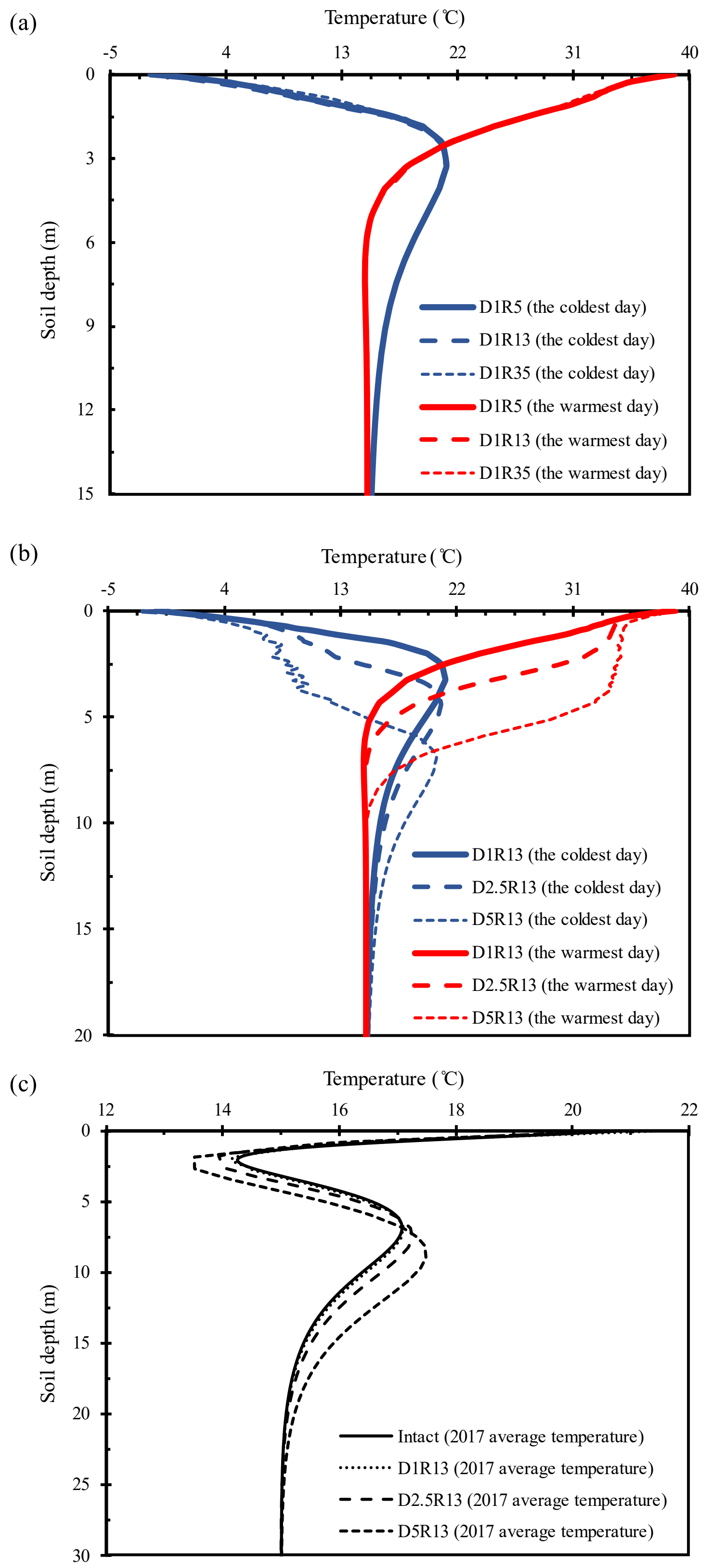

Fig. 9. (a) Crack width and (b), (c) crack depth effects on temperature distribution between 3rd and 4th cracks.

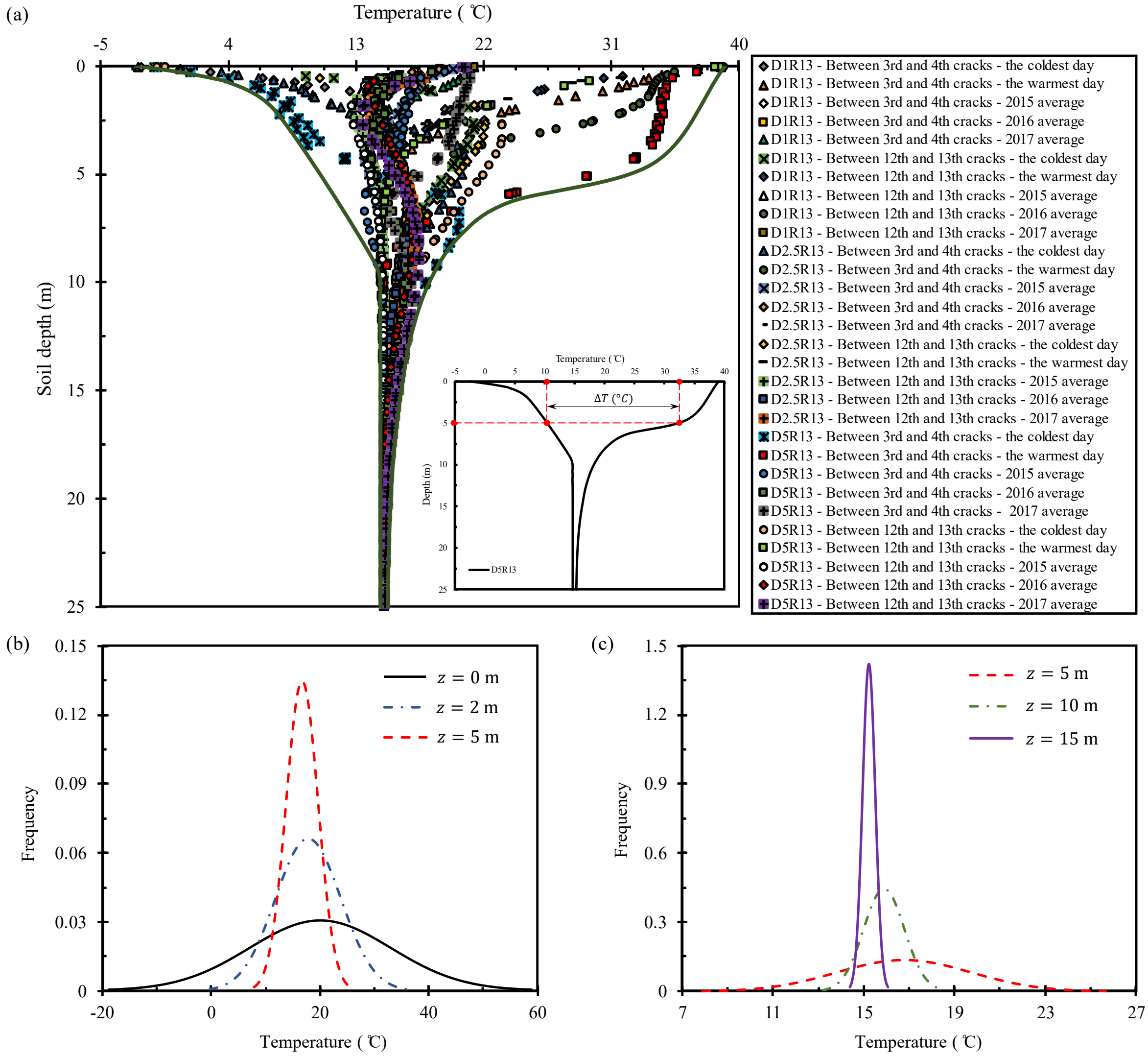

Fig. 10. (a) Variations in temperature for all crack depth and spacing at each climate conditions, and probability density function (PDF) of temperature for different soil depths of (b) 0, 2, 5 m, and (c) 5, 10, 15 m.

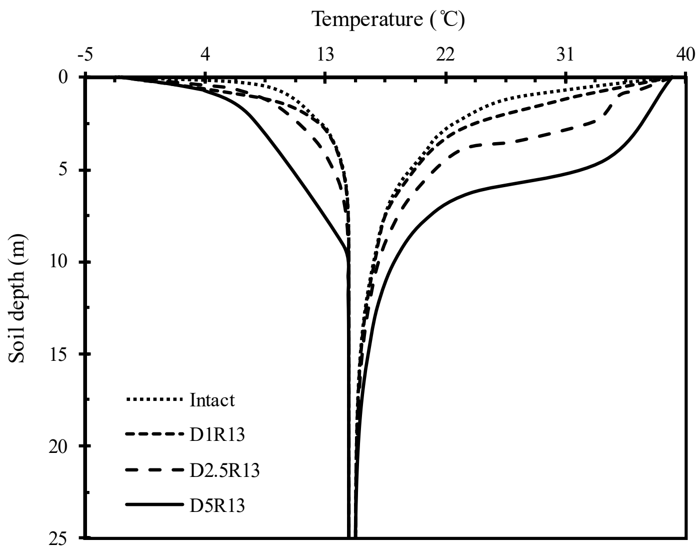

Fig. 11. Variations in temperature for various crack depths.

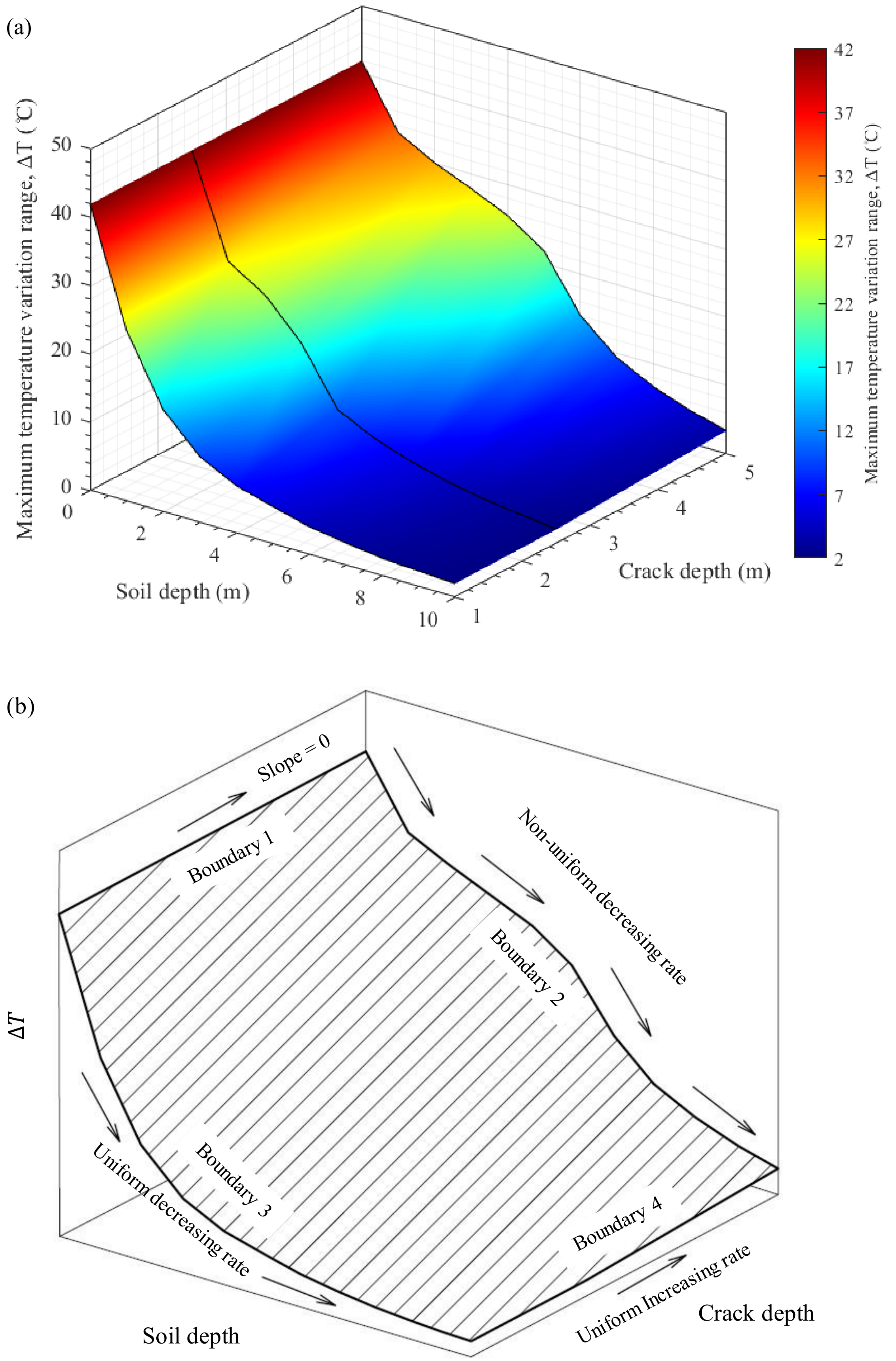

Fig. 12. 3D boundary surface for prediction of the maximum temperature variation against the crack depth and soil depth.

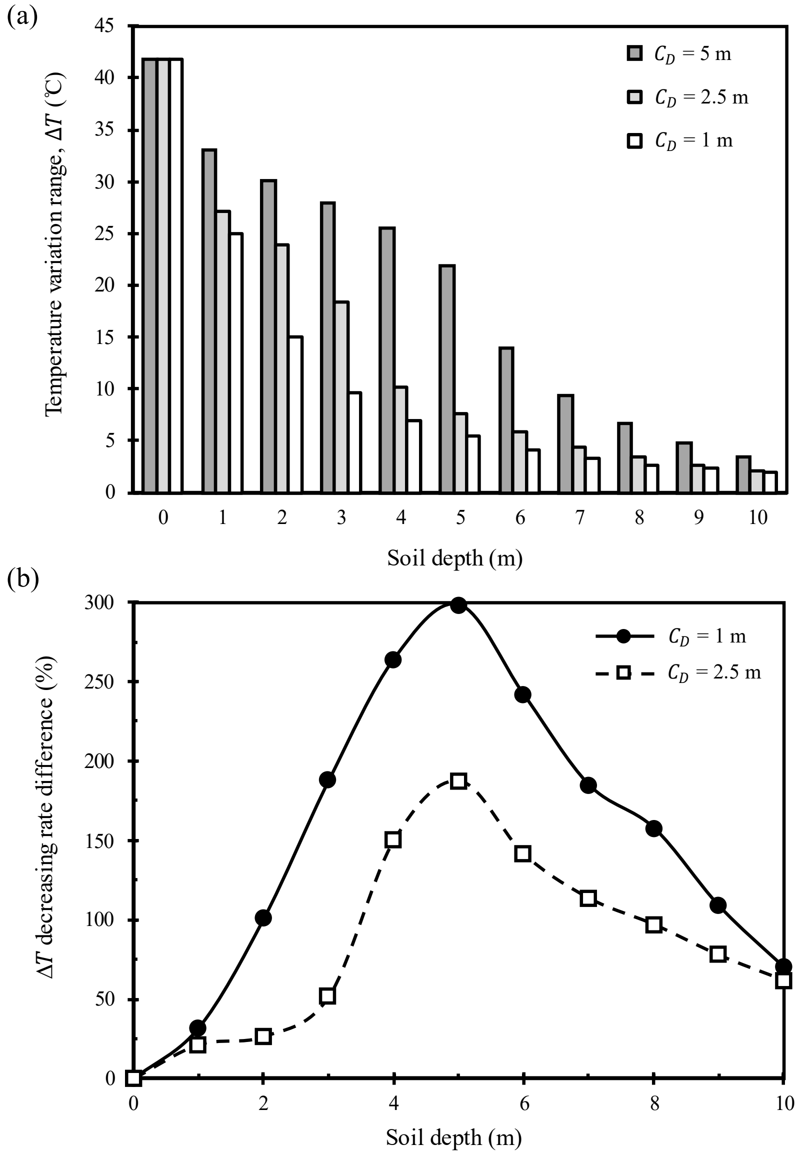

Fig. 13. (a) Difference between ΔT at various soil depths, (b) ΔT decreasing rate difference compared to C_D = 5 m.

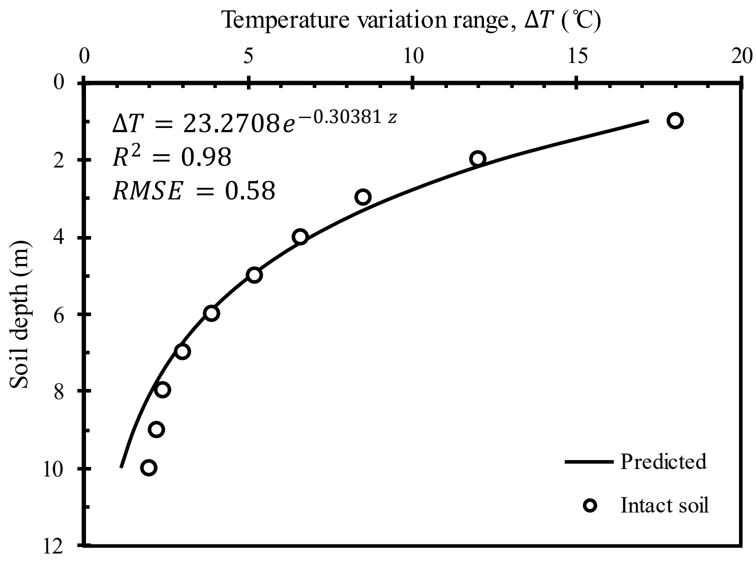

Fig. 14. Variations in temperature in the intact soil, fitted curve and proposed equation.

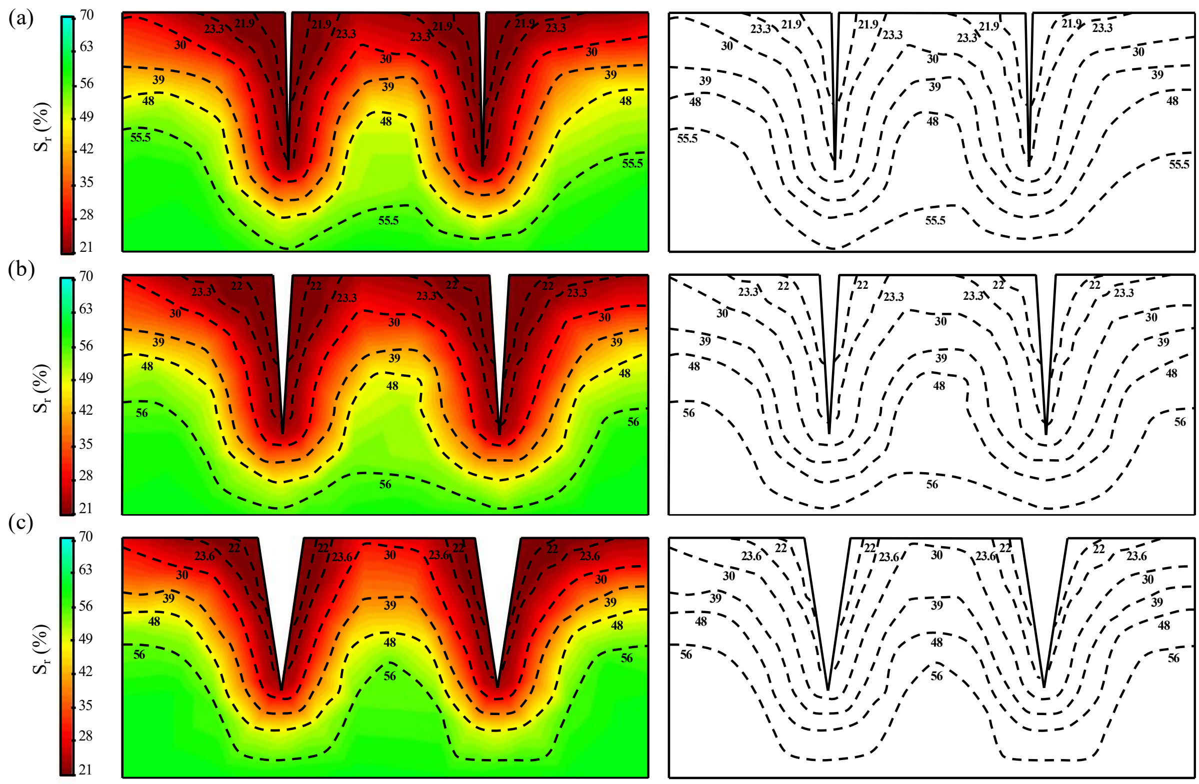

Fig. 15. Two-dimensional distribution of degree of saturation in cracked soil after 3 years, (a) D1R5, (b) D1R13, (c) D1R35 for 3rd and 4th cracks.

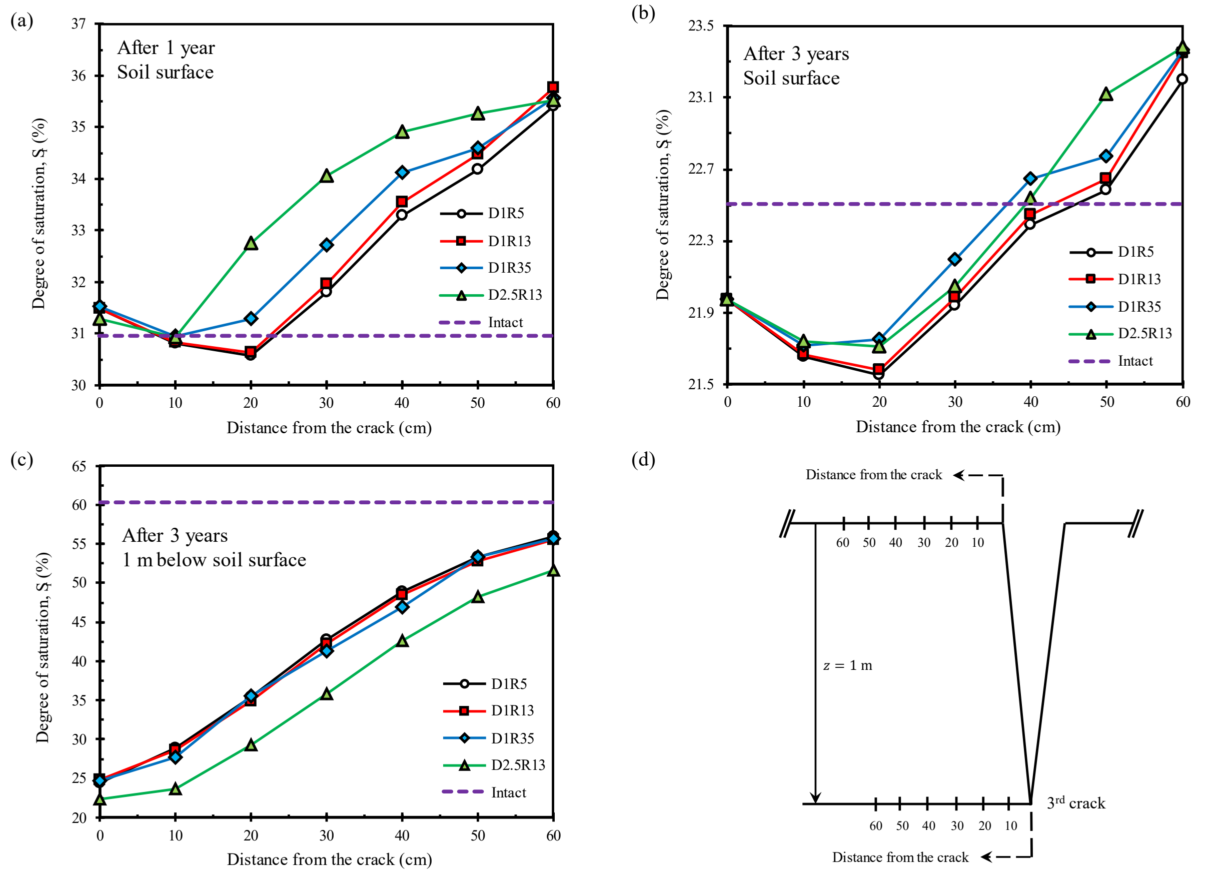

Fig. 16. Drying progress in intact and cracked soil, (a) soil surface drying after 1 year, (b) soil surface drying after 3 years, (c) drying at 1 m depth after 3 years, and (d) schematic diagram defining the distance convention from the 3rd crack.

Table 1

Summary of the constitutive equations and model input values.

Parameter	Description	Value	Equation
Retention curve			
P_0	Measured P at certain temperature (MPa)	3.44	Eq. (6)
σ_0	Surface tension (N/m)	0.072	
λ	Shape function for retention curve	0.3	
S_{rl}	Residual saturation	0	
S_{ls}	Maximum saturation	1	
Liquid phase permeability			
k_0	Intrinsic permeability (m^2)	2.5×10^{-19}	Eq. (5)
λ	Model parameter	0.3	
Gas phase permeability			
A	Constant	1	Eq. (7)
λ	Model parameter	3	
Vapour diffusion			
D	Model parameter (m^2. Pa. s^{-1}. K^{-n})	5.9×10^{-6}	Eq. (9)
n	Model parameter	2.3	
τ_{au}	Coefficient of tortuosity	1	
Heat conduction			
κ_{dry}	Thermal conductivity of the dry porous medium (W/m°K)	0.646	Eq. (11)
κ_{sat}	Thermal conductivity of the water saturated porous medium (W/m°K)	1.4396	

Table 2

Parameters of the crack geometry reported in the previous studies adopted various methodologies.

Crack type	Procedure	C_W (mm)	C_D (mm)	C_R (%)	Reference
Natural	Field observation	50.8 – 76.2	609.6	8.30 – 12.50	[41]
Artificial	Experimental test	6.4 – 19.1	300.0	2.13 – 6.36	[48]
Natural	Field observation	50.0 – 70.0	600.0 – 900.0	7.70 – 8.30	[42]
Natural	Field observation	5.0	400.0 – 500.0	1.00 – 1.25	[43]
Natural	Field observation	N.A.	500.0 – 6000.0	N.A.	[21]
Natural	Field observation	17.0 – 21.0	50.0	34.00 – 42.00	[22]
Natural	Experimental test	10.0	160.0	6.25	[25]
Natural	Field observation	25.0	300.0	8.33	[23]
Natural	Numerical modeling	12.0 – 18.0	300.0	4.00 – 6.00	[31]
Artificial	Experimental test	5.0 – 20.0	50.0 – 100.0	5.00 – 40.00	[44]
Natural	Experimental test	4.5	15.0	30.00	[27]
Natural	Experimental test	0.4 – 1.0	8.0	5.00 – 12.50	[29]
Artificial	Experimental test	4.0 – 10.0	50.0	8.00 – 24.00	[45]

N.A.: Not Applicable

Table 3

Scenarios defined to study the influence of crack geometry.

Name	C_D (m)	C_R (%)	C_W (m)
D1R5	1	5	0.05
D1R13	1	13	0.13
D1R35	1	35	0.35
D2.5R13	2.5	13	0.325
D5R13	5	13	0.65